©Copyright 2019
David Fertitta

Semidiurnal Internal Tides in the Santa Maria Basin

David Fertitta

A thesis
submitted in partial fulfillment of the
requirements for the degree of

Master of Science in Civil Engineering

University of Washington

2019

Committee:

Nirnimesh Kumar

Jim Thomson

Sutara Suanda

Program Authorized to Offer Degree:
Civil and Environmental Engineering

University of Washington

Abstract

Semidiurnal Internal Tides in the Santa Maria Basin

David Fertitta

Chair of the Supervisory Committee:
Assistant Professor Nirnimesh Kumar
Department of Civil & Environmental Engineering

The Santa Maria Basin (SMB) extends from Point Arguello to Point Buchon along the central California coast. This region is subjected to strong wind, wave, and internal tidal forcing leading to complex three-dimensional circulation patterns, material exchange, and density evolution on synoptic and shorter time scales. Previous studies in this region indicate that during summer the semidiurnal internal tidal activity onshore of the shelf break is from internal tidal generation on the continental slope at water depths of h=1000–3000m, with no local generation occurring at the shelf break. However, the length scales over which semidiurnal internal tidal energetics vary within the SMB, along with temporal variability on seasonal and longer time scales, are not yet known.

Here, we use the Regional Ocean Modeling System with a nested grid approach to simulate semidiurnal internal tidal dynamics in the SMB from July to November, 2017. Modeled sea-surface elevation, subtidal and barotropic tidal flows, temperature, and internal tidal fluxes are compared to measurements from the mid- and inner-shelf, obtained as a part of the Office of Naval Research, Inner-Shelf DRI. At 50 m water depth, modeled internal tidal energy fluxes are stronger offshore of Point Sal and Point Purisima but decrease north of Point Sal. Furthermore, internal tidal energy fluxes decay exponentially from 100 to 30 m, with an e-folding length scale of 2.3–2.7 km, consistent with previous observations in the region. Alongshore variability of internal tidal energy fluxes over a length scale of 50 km at

the 50 m isobath are partially attributed to differences from the internal wave field generated offshore, but also due to changing subtidal circulation, submesoscale eddy activity, and stratification. Finally, the internal wave propagation is found to be primarily a progressive wave in the outer-shelf, transitioning to a partial standing wave pattern in the inner-shelf. Funded by the National Science Foundation and the Office of Naval Research.

TABLE OF CONTENTS

LIST OF FIGURES

LIST OF TABLES

ACKNOWLEDGMENTS

I thank all of my friends, family, and colleagues who supported me while producing this thesis. My fellow students in the Environmental Fluid Mechanics group and Civil & Environmental Engineering and my colleagues in the School of Oceanography have provided a great network of mentoring preparing for this thesis. I will always be grateful for the support they provided which has been crucial every step of the way.

Nirnimesh Kumar provided a wonderful opportunity when he took me on as a student. I have learned so much while working with him, and I owe a special debt of gratitude for his support. His passion as a researcher and encouragement as an advisor made this work possible. I would also like Sutara Suanda, Jacqueline McSweeney, Jim Lerczak, Christopher A. Edwards, Seongho Ahn, Kevin Haas, Arthur Miller, and Emanuele Di Lorenzo for their contribution to this project.

I would additionally like to thank Jen MacKinnon, Amy Waterhouse, Joe Calantoni, and John Colosi for providing mooring observational data. This work was supported by the Office of Naval Research (ONR) Littoral Geosciences and Optics Program (Code 321), and I received additional supported from the National Science Foundation (NSF) Graduate Research Fellowship Program (GRFP).

Chapter 1

INTRODUCTION

Internal (baroclinic) waves are waves in the ocean interior occurring in stratified waters and are generated by isopycnal displacements. Because they exist between between layers of warmer, less-dense water and colder, denser water, internal waves have a big impact on circulation and vertical mixing in the ocean [e.g., *Munk and Wunsch*, 1998; *Wunsch and Ferrari*, 2004; *Ferrari and Wunsch*, 2009; *Waterhouse et al.*, 2014]. The impact of internal waves on large-scale ocean mixing can, in turn, impact climate processes [e.g., *MacKinnon et al.*, 2017; *Whalen et al.*, 2018]. Internal waves can also impact offshore marine structure stability [*Osborne et al.*, 1978] and acoustic signals [*Dushaw et al.*, 1995; *Ramp et al.*, 2004]. Barotropic tidal processes are the dominant driving mechanism behind internal waves.

Internal waves generated at tidal frequencies are referred to as internal tides and correspond to isopycnal displacements from interaction of the astronomical (barotropic) tide with ocean bottom topography in stratified waters. This generation can occur in the deep ocean [*Simmons et al.*, 2004; *Garrett and Kunze*, 2007], propagate over length scales that of an ocean basin [*Zhao et al.*, 2010], transport the energy associated with it over long distances [*Alford*, 2001; *Waterhouse et al.*, 2018], and reach distant locations in coastal waters [*Martini et al.*, 2011; *Kerry et al.*, 2013]. Furthermore, internal tidal generation may also occur along the continental shelf [*Nash et al.*, 2012a]. Internal tides are ubiquitous in coastal oceans throughout the world [*Jackson and Apel*, 2004].

The inner- to mid-shelf (∼5–50 m water depth) region of the coastal ocean is highly dynamic and often acts as a transition zone between the deeper ocean to the edge of the surf zone (region dominated by surface wave breaking). Here, surface wave, wind, and tidal forcing lead to complex circulation dynamics and determine material exchange [*Lentz*

and Fewings, 2012]. The role of wind- and wave-driven circulation and associated material exchange has been studied through field measurements [e.g., *Fewings et al.*, 2008; *Lentz et al.*, 2008; *Horwitz and Lentz*, 2014, 2016] and numerical models [e.g., *Austin and Lentz*, 2002]. It is only recently that researchers have investigated shelf variability due to internal tidal processes.

Upon reaching shallower waters near the coast, internal tides shoal and break leading to intense mixing of coastal waters [*Sinnett et al.*, 2018] modifying biological processes [*Woodson*, 2018]. The shoaling internal waves can cool or warm surface waters [*Pineda*, 1991; *Walter et al.*, 2014], decrease dissolved oxygen levels in nearshore waters [*Frieder et al.*, 2012; *Walter et al.*, 2014], can induce material transport such as larvae [*Pineda*, 1991; *Lucas et al.*, 2011] and pollutants [*Boehm et al.*, 2002], and can bring nutrients to the surface [*McPhee-Shaw et al.*, 2007; *Roder et al.*, 2010] which may lead to harmful algal blooms [*Omand et al.*, 2011]. It is therefore critical to be able to measure the signal corresponding to internal tidal variability.

Internal tides are observed in the ocean using moored temperature and velocity measurements to understand the variability of energy [e.g., *Sherwin*, 1988] and vertical structure [e.g., *Pickering et al.*, 2015]. Even though internal tides exist in the ocean interior, their surface signal is observed using satellite remote sensing to understand their spatial variability [e.g., *Zhao et al.*, 2010].

Prior observations on the continental shelf indicate variability of internal tides from offshore to nearshore [*Lerczak et al.*, 2003; *Rayson et al.*, 2011; *Suanda and Barth*, 2015] and that remotely-generated internal tides can cause mixing in coastal waters [e.g., *Waterhouse et al.*, 2017]. Complex bathymetry, such as a submarine canyon, has been seen to increase the variability of internal tides regarding dissipation and the standing vs. propagating nature of internal waves [*Waterhouse et al.*, 2017].

The complex role that internal tides play in coastal waters makes it crucial to understand better the variability of their dynamics. Regional ocean modeling has been shown to be a useful tool for studying internal tides [*Carter et al.*, 2012]. However, modeling internal tides is

challenging as they can be generated locally on the continental shelf or in the open ocean and then propagate onto the continental shelf [*Nash et al.*, 2012a, b]. Internal tides generated in the open ocean are in general not in phase with the locally-generated internal tides [*Buijsman et al.*, 2012], and regional numerical models often do not include internal tidal signal from the open ocean. Previous modeling efforts have involved idealized simulations to study energetics and effects on mixing [*Chen et al.*, 2003] and circulation [*Kurapov et al.*, 2010], or have been used to study internal tides in deeper waters [e.g., *Kerry et al.*, 2013, 2016].

Most of these simulations are hydrostatic—an approximation valid for internal tides in the open ocean. However, in water depths closer to shore, internal tidal wavelengths are 100 m, and the horizontal and vertical length scales are of the same order of magnitude. Therefore, the hydrostatic approximation may be invalid, and it becomes necessary to use nonhydrostatic formulations which accurately simulate processes on similar horizontal and vertical length scales [*Vitousek and Fringer*, 2011]. However, nonhydrostatic models (e.g., MITgcm, SUNTANS) are computationally expensive to run [*Fringer et al.*, 2006] and cannot be used for large spatial scales. Yet idealized simulations and applications for smaller spatial domains near the coast and coupling with hydrostatic models have been considered [e.g., *Choboter et al.*, 2016; *Garcia et al.*, 2019].

Even though some efforts have focused on validating observed semidiurnal internal tides on the shelf region [e.g., *Kumar et al.*, 2016, 2019], the applicability of numerical models to represent internal tidal variability on length scales of 50 km or more is not yet considered and is the focus of this work, which is augmented by observations from the Santa Maria Basin (SMB). The Office of Naval Research funded an Inner Shelf experiment in the SMB from September–November, 2017 [e.g., *Lerczak et al.*, 2019] which expands upon a 2015 pilot experiment in the same region [e.g., *Colosi et al.*, 2018]. Whereas the 2015 pilot study deployed moorings offshore of Point Sal, CA without much alongshore variation [*Colosi et al.*, 2018], the 2017 full experiment deployed additional moorings to the north and to the south of Point Sal (a 7.5-km headland) to investigate both cross-shore and alongshore variability of internal tides.

The SMB is a region extending from Point Buchon to Point Arguello along the central California coast where complex bathymetry leads to complex circulation patterns. Point Buchon—a 28-km wide headland at the northern end of the SMB—and the mountains nearby shadow the shelf from the prevailing winds from the north, which creates an alongshore gradient in wind stress and wave energy. The SMB is also impacted by episodic plumes of warm water from southern California [*Washburn et al.*, 2011; *Fewings et al.*, 2015; *Suanda et al.*, 2016], which alters local circulation and stratification.

Here, we investigate temporal and spatial variability of the semidiurnal (M_2, period of 12.42 hours) internal tide in the SMB. The observations are complemented with a nested regional ocean model to validate models for horizontal scales of 50 km and to be used in future studies modeling internal tides on longer temporal scales. Variability of internal tides from Point Conception to 100 km alongshore is not known, even though subtidal variability has been studied [e.g., *Fewings et al.*, 2015]. Furthermore, internal tidal propagation characteristics are not known these length scales.

Chapter 2

METHODS

2.1 Inner Shelf DRI

To understand better the dynamics of the inner shelf on horizontal length scales of ∼50 km, the Office of Naval Research funded a multi-institutional inner shelf Departmental Research Initiative (DRI). The field experiments in the DRI focused on the Santa Maria Basin (SMB) off the coast of Point Sal, California near Vandenberg Air Force Base. The location of Point Sal was chosen due to its complex bathymetry alternating between rocky outcrops (e.g., Point Sal, Point Purisima) and relatively straight, sandy west-ward facing beaches (Figure 2.1). Here, physical processes interacting with seafloor and coastline features lead to spatially and temporally varying three-dimensional dynamics impacting circulation and stratification in the SMB. For example, flow separation associated with coastline features may lead to eddy activity and fronts with varying length and decorrelation time scale along the coastline. The shelf stratification in SMB can change due to temperature variability associated with upwelling-favorable winds and relaxation events, which bring warmer Santa Barbara Channel waters to the study region [e.g., *Washburn et al.*, 2011; *Suanda et al.*, 2016]. The internal tidal variability associated with changing stratification on synoptic timescales is not yet known for the central California region.

Measurements taken during the fall 2017 experiment include acoustic Doppler current profiler (ADCP) and temperature chain (T-chain) moorings, shipboard surveys, drifters, meteorological buoys, X-band radar, and airborne visible and infrared (IR) imagery remote sensing [e.g., *Lerczak et al.*, 2019]. In addition to observations, numerical modeling studies complement in understanding the dynamics where observations where not taken such as locations farther offshore. Having both observations and model outputs will provide a more

thorough understanding of the alongshore and cross-shore variability of internal tides on the central California coast as internal tides both in the inner shelf and in deeper waters throughout the SMB can be investigated. The approximately 2-month observational period combined with an alongshelf and cross-shelf spread of instruments allows for investigating both temporal and spatial dynamics of internal tides in the SMB.

2.2 Observations

2.2.1 Moorings

Moorings with measurements of both temperature and velocity during the Innershelf DRI were used to investigate internal tidal dynamics in the Santa Maria Basin. For comparison to the Regional Ocean Modeling System (ROMS), the moorings between 30m and 100m depths were used. Observations in water depths <30 m were not considered since ROMS uses the hydrostatic approximation, and this approximation breaks down in shallower depths—as the horizontal and vertical scales of motion become similar order of magnitude. A map of the location of the moorings fitting this criteria are shown in Figure 2.1 (colormap used here—and in each figure with a colormap—described in *Thyng et al.*, 2016).

Since the vertical resolution of the temperature measurements (∼2–3 m vertical spacing) was coarser than the velocity measurements (∼1–2 m bin size depending on the mooring), the temperature and velocity measurements are interpolated to the same evenly-spaced z-grid [e.g., *Suanda et al.*, 2011]. To ensure that the calculation of internal tidal parameters is consistent over a changing depth due to tidal elevation, the temperature and velocity measurements were the interpolated to a σ-grid using the observed sea surface height where, for each time step, the sigma coordinates are evenly-spaced vertically. In instances where instruments did not measure all the way to the surface or bottom, the observational data was extrapolated to the surface and/or bottom. After extrapolation to the surface and bottom, the values of velocity and temperature measurements are averaged every hour to match the frequency of the hourly model outputs. Observed velocities were rotated into principal axes.

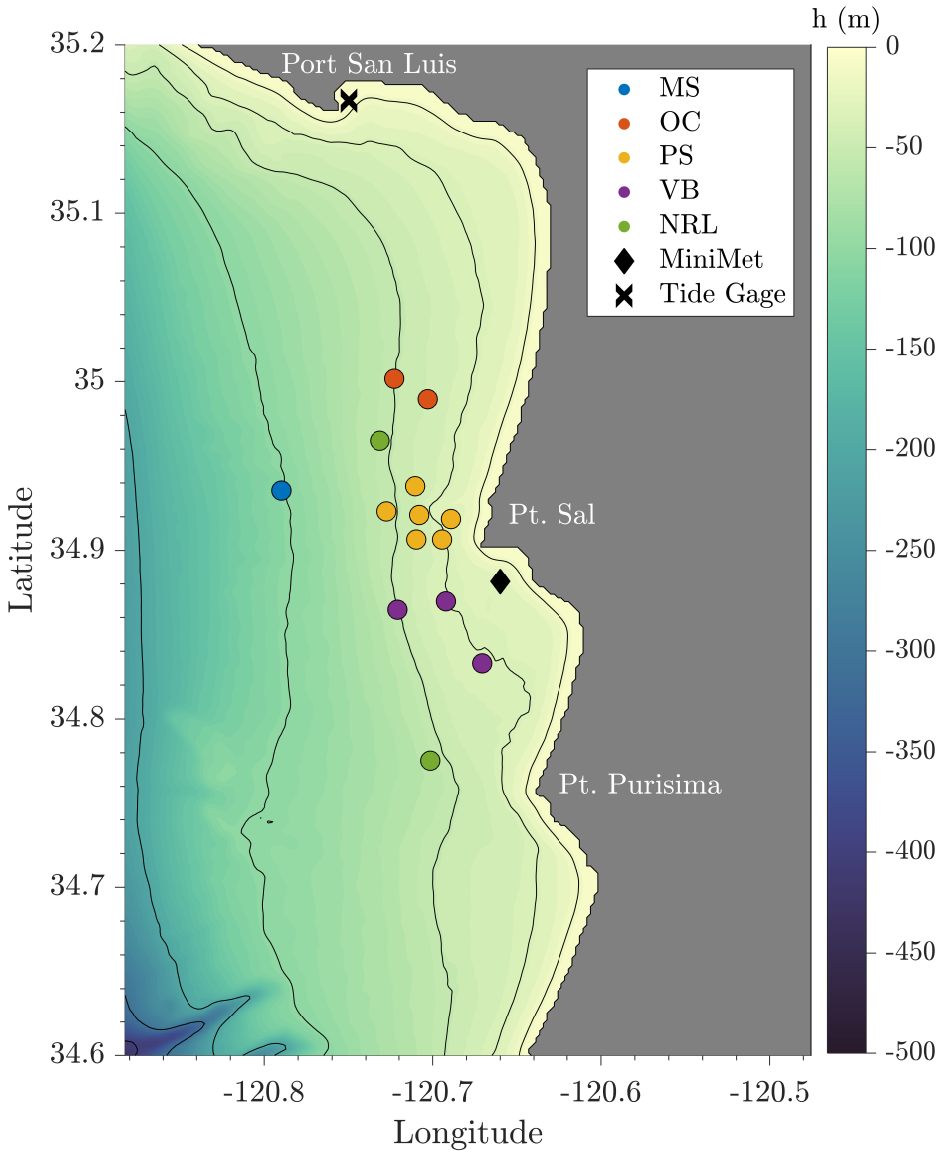

Figure 2.1: Bathymetry used in the model simulation with a 200m horizontal resolution indicated by the colormap. Location of moorings (colored circles) with observations of temperature and velocity deployed during Point Sal ISDRI, 2017. Each mooring is color-coded to the array of deployment in which it belongs: mid-shelf (**MS**), Oceano (**OC**), Point Sal (**PS**), Vandenberg (**VB**), and Naval Research Lab (**NRL**). Black diamond indicates location of onshore weather buoy (MiniMet station), and the black x indicates the location of the tide gage at Port San Luis. Solid black lines are bathymetry contours of 400, 300, 200, 100, 50, 30, 10 m water depth.

2.2.2 Meteorology

Meteorological observations of tidal elevation and offshore wind velocities during the deployment period of the Innershelf DRI are shown in Figure 2.3. Mean sea level measurements were recorded at tide gage 9412110 at Port San Luis, CA (35.167°N, 120.75°W; Figure 2.1). Offshore wind velocities were recorded at NOAA station 46011 (34.956°N, 121.019°W; Figure 2.2). Onshore wind velocities were recorded at a Mini Met buoy (34.8814°N, 120.6599°W; Figure 2.1) just south of the headland at Point Sal—the lee side of the prevailing wind direction in the SMB.

The tides in this region are dominated by the M_2 tide (Figure 2.3). Low-pass filtering (periods >33 hours) the winds allows for looking at the subtidal (scale of days to weeks) winds (Figure 2.3). The prevailing wind direction is mostly to the south and are upwelling-favorable. Events when the north-south component of subtidal (days to weeks) wind magnitude is small or the direction is opposite from the prevailing wind direction are known as wind relaxation events and can introduce warm waters from the Santa Barbara channel to the SMB [*Cudaback et al.*, 2005; *Suanda et al.*, 2016]. The first month of the observational period has different atmospheric dynamics than the second month as the relaxation events are more pronounced in the first month but occur more frequently in the second month of the deployment period.

2.3 Numerical Model

The numerical model used in this study is the open-source Rutgers Regional Ocean Modeling System (ROMS). ROMS is a three-dimensional numerical model that uses a terrain-following cooordinate system and a finite-difference scheme to solve the Reynolds-Averaged Navier-Stokes Equations with hydrostatic (scale of horizontal motion is at least an order of magnitude higher than the scale of vertical motion) and Boussinesq approximations [*Shchepetkin and McWilliams*, 2005, 2009]. A series of nested grids [e.g., *Suanda et al.*, 2016, 2017] was used starting with a simulation covering much of the northeast Pacific (L0, $\Delta x = 3$ km) and modeled the dynamics over a sequentially smaller spatial area: L1 has $\Delta x = 1$ km, L2 has

$\Delta x = 600$ m, and L3 has $\Delta x = 200$ m. This framework allowed for resolving processes at the open-ocean to inner-shelf scale and to capture both larger-scale spatial variability and high-resolution results in the SMB near Point Sal, CA. The bathymetry for grids L2 and L3 are from NOAA-NCEI Coastal Relief Model dataset with 1 arc-second resolution. The bathymetry of the L2 nested grid is shown in Figure 2.2, and the L3 nested grid bathymetry with mooring locations overlaid on top is shown in Figure 2.1.

Model simulations were run from 01-July-2017 to 17-Nov-2017 with hourly output of model variables. The first two nested grids (L0 and L1) do not simulate sea surface elevation or barotropic velocities associated with the tides. Barotropic (astronomical) tides (astronomical constituents K_2, S_2, M_2, N_2, K_1, P_1, Q_1, N_1 as well as the over-tides M_4, M_6) were added at the western and southern boundaries of the L2 grid, and the model uses neither data-assimilation nor forcing of remotely-generated internal tides. Therefore, any modeled baroclinic (internal) tidal processes are generated within the L2 grid domain or the subsequent nested child grid, L3. The L3 grid features a terrain-following coordinate system with 42 vertical layers, 0.1 $m^2\ s^{-1}$ for horizontal eddy viscosity, and k-ϵ model for eddy diffusivity. All model outputs of temperature and velocity for comparison with the mooring observations are taken from the L3 grid.

The L0 grid is initialized with World Ocean Atlas climatological lateral boundary conditions, and each one-way offline nest receives its boundary conditions from the parent grid. For the barotropic field, radiation boundary conditions were used to allow energy to leave the domain [*Flather*, 1976; *Chapman*, 1985; *Mason et al.*, 2010], and for baroclinic velocity and temperature, both radiation and nudging [*Marchesiello et al.*, 2001] boundary conditions are used. Incoming baroclinic velocities and tracers are nudged on a 1-hour time scale (strongly), and outgoing baroclinic velocities are nudged on 1-year time scale (weakly).

2.3.1 Model Atmospheric Forcing

The Coupled Ocean-Atmosphere Mesoscale Prediction System (COAMPS) numerical model was run ($\Delta x \sim 9$km) over the northeast Pacific Ocean [*Hodur et al.*, 2002]. Modeled wind

velocities were extracted at the location of two buoys (one offshore: Figure 2.2; one onshore: Figure 2.1). A comparison of the COAMPS forcings to buoy observations at the two buoys locations is shown in Figure 2.4. Overall, the COAMPS winds have good model-data at the offshore location and larger differences occur at the onshore location which lies in the lee side of the headland at Point Sal.

2.4 Estimation of Internal Tidal Parameters

To quantify variability in internal tidal energy, the baroclinic pressure and velocities were used to calculate values for baroclinic energy fluxes, available potential energy (APE), and horizontal kinetic energy (HKE).

2.4.1 Calculate Background Density and Stratification

The background stratification was calculated over a moving window with a time period of 25 hours (fully encompassing two tidal cycles for the semidiurnal tide period of 12.42 hours given the limitation of hourly model outputs), and the window of calculation shifts forward every 5 hours so that the calculation window is an integer multiple of the time shift. The background density was computed by sorting the water column density [*Winters et al.*, 1995]. Within each 25-hour period, the density for each sigma layer was placed into one vector. Then, the densities were sorted in descending order, and any remaining common values were removed. This sorted profile was used as the reference density for the given 25-hour time period. The stratification is quantified using the Brunt-Väisälä Frequency

$$N^2 = -\frac{g}{\rho_0}\frac{\partial \rho}{\partial z}$$

where ρ is the reference density and ρ_0 is the depth-averaged density at this timestep.

2.4.2 Baroclinic Velocity and Pressure

The velocities are filtered to include only the signal with periods between 1 and 16 hours to look at the energetics from the semidiurnal band and higher frequencies. The baroclinic

velocity perturbation $\mathbf{u}'$ is calculated by subtracting the mean filtered velocity $\overline{\mathbf{U}}$ from the filtered velocity. Similarly, the baroclinic pressure perturbation p' is calculated by subtracting the mean filtered pressure from the filtered pressure. When the baroclinic velocities and pressure are integrated with depth, the results should equal zero [e.g., *Nash et al.*, 2004].

2.4.3 Calculation of Baroclinic Energy Fluxes

The baroclinic energy fluxes, available potential energy (APE), and horizontal kinetic energy (HKE) are calculated over the same 25-hour time period with a shift of 5 hours as in the calculation for the background density and stratification. The HKE is then found using the equation

$$HKE = \frac{\rho_0}{2} \int_{z=-h}^{\eta} \left(u'^2 + v'^2 \right) dz,$$

where $\rho_0 = 1025$ kg m^{-3}. Within each 25-hour period, the densities from each sigma layer were placed into one vector and sorted in descending order to create the background reference stratification.

For each depth, the fluid parcel reference vertical position z_* is computed. Then, the difference between the potential density and reference density $\rho(z - z_*)$ is computed, which gives

$$APE = g \int_{z=-h}^{\eta} \rho(z - z_*) dz.$$

Next, the pressure is calculated and the mean pressure is removed to find the baroclinic pressure perturbation p'. The energy fluxes are computed by multiplying $\mathbf{u}'$ by p'. To find the baroclinic energy flux at a given time, the baroclinic velocity and pressure are integrated with depth as in

$$\vec{F} = \int_{z=-h}^{\eta} \mathbf{u}' p' dz.$$

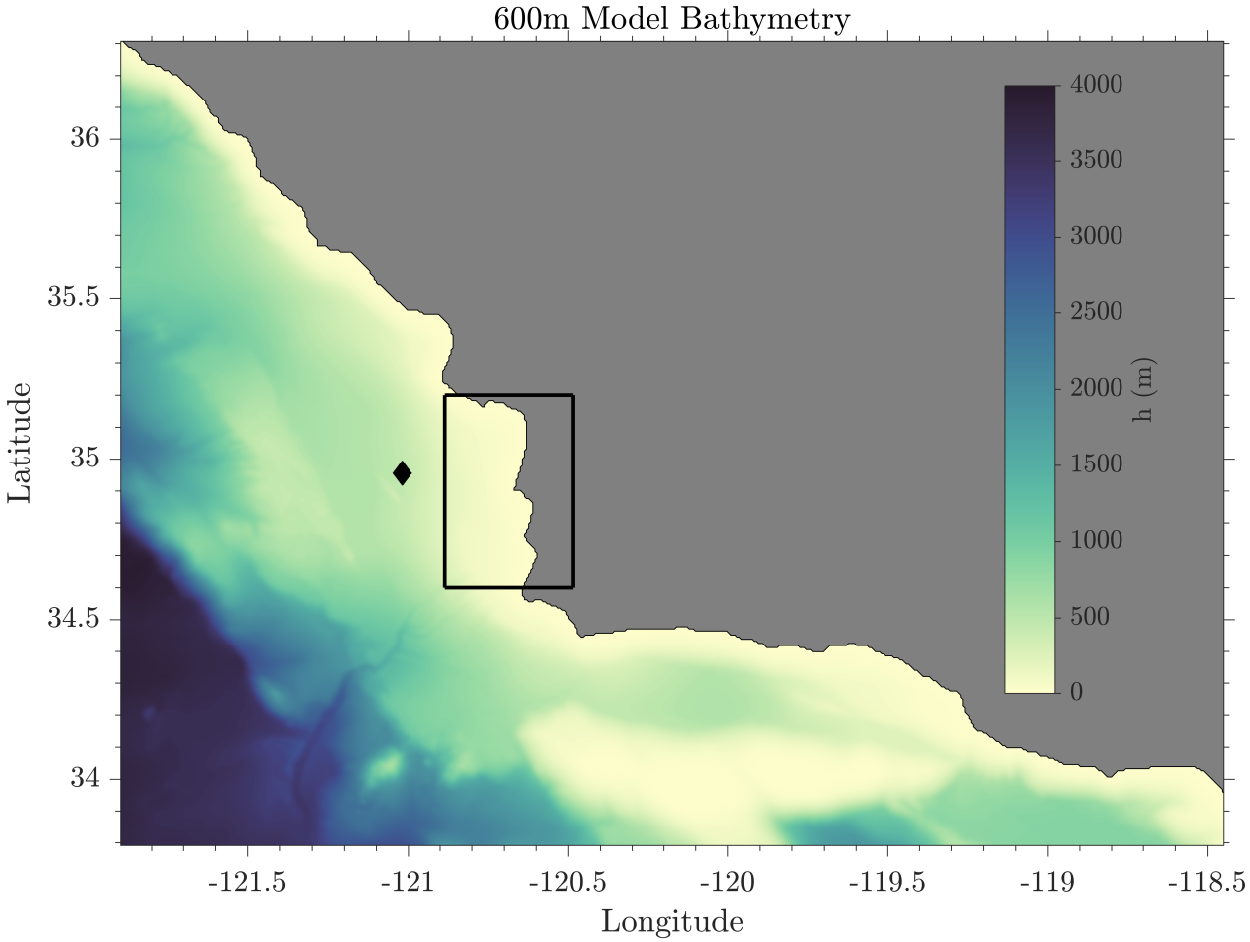

Figure 2.2: Bathymetry used in the model simulation with a 600 m horizontal resolution (L2) indicated by the colormap. Barotropic tides added at the western and southern boundaries of this grid. Black diamond indicates location of offshore weather buoy (NOAA 46011), and the black box indicates the boundary of the L3 grid.

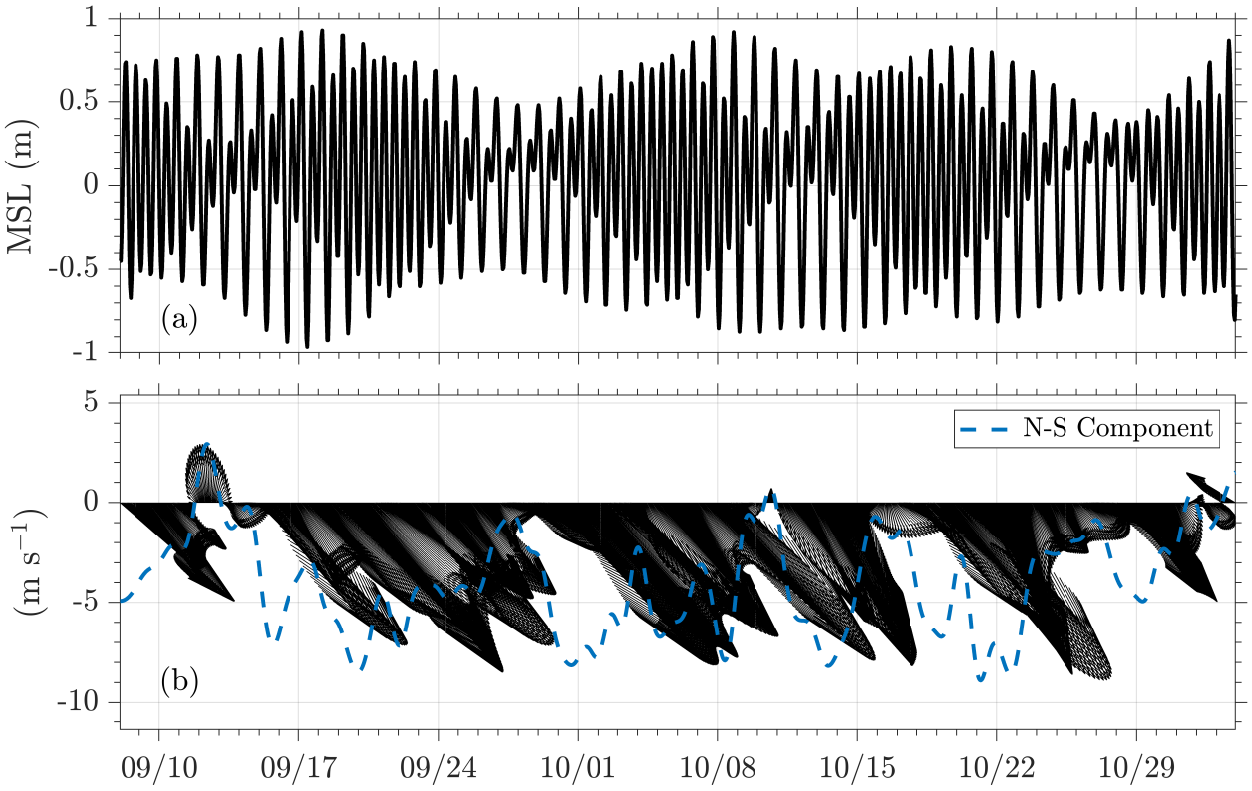

Figure 2.3: Sea surface elevation (top) and wind velocity (bottom) vs. time at Port San Luis, CA, and NOAA 46011, respectively. North-south component of wind indicated by dashed line.

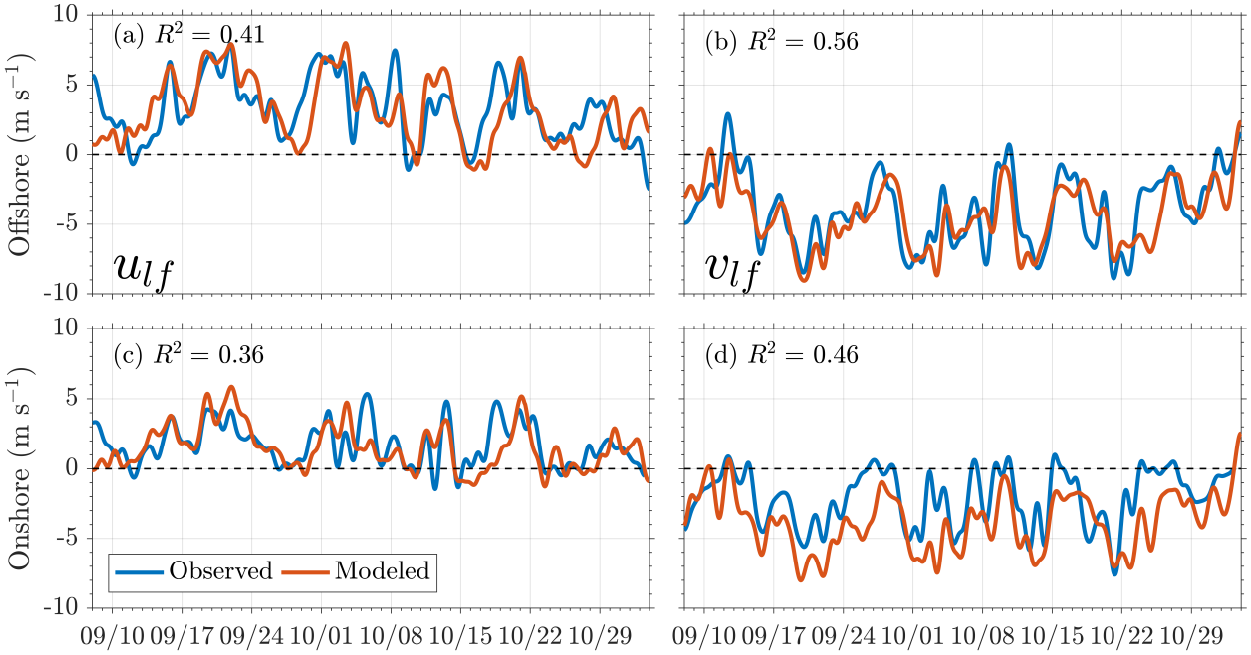

Figure 2.4: Comparison of observed (blue line) and modeled (COAMPS, red line) subtidal (period >33 hours) winds for an offshore buoy (NOAA 46011, top panels) and an onshore buoy (MiniMet, bottom panels) for wind speeds in the east-west direction (left panels) and north-south (right panels) direction.

Chapter 3
MODEL-DATA COMPARISON

ROMS has not been previously tested against observations at length scales of 50 km. Before investigating the baroclinic subtidal and tidal processes, it is important to understand how well the model captures the barotropic processes in comparison to the observations as both drive and modify baroclinic processes. To explore the subtidal dynamics, modeled velocities and temperature were extracted at the location of each of the 14 moorings deployed in the SMB indicated in Figure 2.1, and comparison of the modeled sea surface elevation was compared to a tide gage at Port San Luis.

3.1 Tidal Comparison

Since the baroclinic tides are forced by the barotropic tides, it is important that the model accurately represents the barotropic tides. A comparison of observed and modeled amplitude and phase for the K_1, O_1, N_2, M_2, and S_2 components of the barotropic tide are shown in Figure 3.1 calculated with the T_TIDE package [*Pawlowicz et al.*, 2002]. The modeled amplitude tends to be slightly higher ($\sim$0.01–0.03 m) than observed tidal amplitudes for each constituent. For the phases, the model is within $\sim 10^{\circ}$ of the observations.

3.2 Temporal Comparison

To investigate subtidal dynamics, the subtidal temperature and velocities are found by low-pass filtering the time series of these variables to retain the signal with a period >33 hours. An example of time-varying profile of subtidal temperature vs. depth and time-varying depth-averaged subtidal north-south velocities at the mooring farthest offshore (**MS100**) is shown in Figure 3.2.

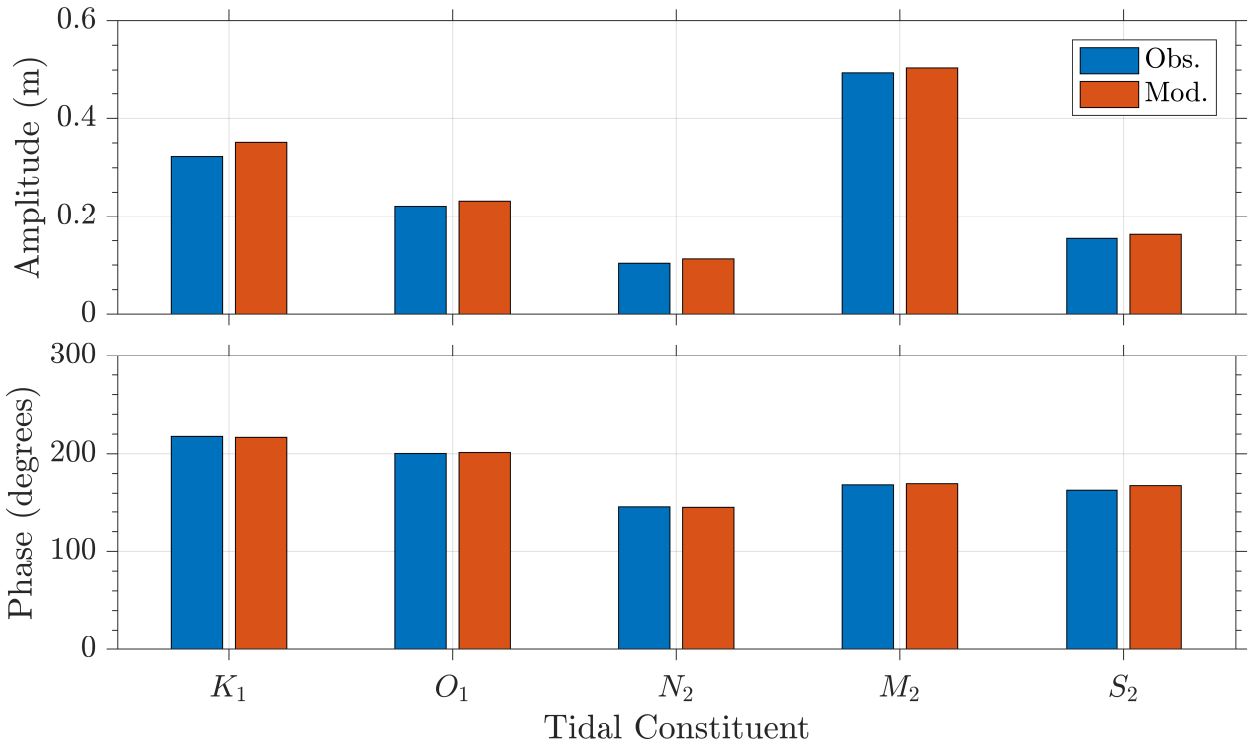

Figure 3.1: Observed (blue) vs. modeled (red) tidal amplitude (top) and phase (bottom) throughout the deployment. Observed tides are from a tide gage at Port San Luis, CA, and the modeled sea surface elevation is from the L3 grid.

The observed near-surface temperatures range from ∼13–18°C. The mean vertical variation of temperature (Figure 3.3) in the observations are from ∼15.5°C at the surface to ∼10.5°C at depth. The modeled near-surface temperatures vary form ∼14–18°C and are consistently warmer than observations. The model mean temperature varies from ∼17°C at the surface (∼1.5°C) warmer than observations) and ∼10.5°C (equivalent to the observations).

Evident is an overall warm bias to the model. While the model is warmer than the observations, the model captures the variations in near-surface temperature as well as the changes in stratification. The increases in near-surface temperature are associated with the wind relaxation events in Figure 2.3, and the model is resolving the circulation effects of those meteorological events. Apparent in Figure 3.2 panel (b) is an exaggerated modeled upward extent of cold water from the bottom entering the rest of the water column not seen in the observations in panel (a). The timing of this is associated with an event with increased upwelling-favorable winds shown in Figure 2.3 beginning around October 21.

The subtidal depth-averaged velocities in panel (c) have an R^2 of 0.32, root mean square error (RMSE) of 0.15 m s^{-1}, and bias of 0.09 m s^{-1}. The model captures many of the broad changes in velocity; however, the model overestimates some of the southward flow and underestimates northward flow. The modeled depth-averaged north-south component of velocity in panel (c) shows that during this event, the model overestimates the extent and duration of southward flow of water causing the modeled over-exaggerated cold water throughout the water column. This effect of this modeled event is seen in the time-averaged temperature vs. depth in Figure 3.3 as the mean modeled temperature is much closer to the observed value at depth.

At a mid-shelf mooring (**OC50**, the northernmost mooring on the 50 m isobath), similar results are seen in the subtidal temperature vs. depth and depth-averaged subtidal north-south velocities as shown in Figure 3.4. The velocities are similarly correlated ($R^2 = 0.28$) but feature a smaller RMSE (0.09 m s^{-1}) and bias (0.03 m s^{-1}) than in deeper waters. The warm model bias between observations and model is still apparent at this location in

shallower waters but is slightly less-pronounced as in deeper waters, but here the model does a better job of not overestimating the velocities. The temperature variability in the cross-shore direction is indicated in Figure 3.6. The warm model bias is more consistent in water depths shallower than 50 m as the effect of the enhanced-upwelling event is less apparent from offshore to nearshore. The modeled exaggerated upwelling is also still apparent at **OC50**; however, the upward extent of cold water is closer to what is seen in observations. At this location, the modeled southward flow during the upwelling-favorable wind event around October 21, 2017 is also closer to what is observed. Similarly, the effect of this modeled event is less in the time-averaged temperature vs. depth in Figure 3.5 than farther offshore as the bias between mean modeled and observed temperature is consistent throughout the water column.

3.2.1 Deployment 1 vs. 2

While some observations have a continuous record of observations throughout the DRI, many of the ADCP and T-chain measurements were deployed and recovered and then re-deployed around the same time for about one month in each deployment. For this analysis, the first deployment period was defined as 08-Sep-2017 to 05-Oct-2017, and the second deployment period was defined as 08-Oct-2017 to 03-Nov-2017. This discontinuity in the observation record occurred in early October and is an artifact of ocean observation difficulties, there were also notable differences in the meteorology as the conditions began to change from summer to fall.

As seen in Figure 2.3, the first deployment exhibited more pronounced—but fewer—wind relaxation events than the second deployment period. Deployment 2 had more wind relaxations that were fairly weak and contained strong upwelling-favorable wind events.

In general, the sea surface temperature (SST) was warmer during the first deployment period and cooler in the second deployment period as indicated by sample snapshots of satellite-derived SST and modeled near-surface temperatures (Figures 3.7 and 3.8), where SST ranges from 17–21°C in the snapshot from September and from 15–18°C in the snapshot

from October.

3.3 Spatial Comparison

Having 14 different moorings spanning waters from 30–100 m deep and covering an ∼25 km distance alongshore provides the opportunity to study multiple physical processes both along the and across the inner shelf and how well ROMS models these processes. For instance, one question lies in how physical processes might differ to the north and south of the headland at Point Sal. This allows allows to see how well ROMS captures dynamics in both shallower and deeper waters. Here, barotropic and subtidal processes will be explored spatially across all 14 moorings deployed during the DRI.

To spatially compare the subtidal velocities, the ellipses for principal axis velocities were found by taking the standard deviation of the subtidal depth-averaged major and minor axis velocities. The observed vs. modeled ellipses of principal axis subtidal depth-averaged velocities at each mooring location are shown in Figure 3.9. The orientation of the principal axis flow at each mooring location is shown in Table 3.1 in addition to the standard deviation of the velocities. The subtidal major axis velocities are somewhat stronger in the model than what is seen in observations overall, but the model slightly underestimates the minor axis velocities. Therefore, the modeled ellipses are more elliptic in shape and the observed ellipses are more circular. In general, the observed subtidal flow more closely follows the bathymetry contours than the modeled velocities and the orientations of the major axes in the model are more north-south, which could be due to the model bathymetry being too smooth. The orientations of the ellipses from the modeled velocities are consistent in the alongshelf direction and do not vary much to the north or south of Point Sal.

To examine the barotropic processes, the package T_TIDE [*Pawlowicz et al.*, 2002] used the complex time series of the depth-averaged velocities at each mooring to calculate the major and minor axis velocities, phase, and inclination of the M_2 tide. The observed and modeled ellipses of principal axis barotropic tidal velocities at each mooring location are shown in Figure 3.10, and the calculated statistics are shown in further detail in Table 3.2.

Table 3.1: Observed and modeled standard deviation for major axis velocities, standard deviation for minor axis velocities, and ellipse inclination (orientation in degrees counter-clockwise positive from east). Statistics calculated from the principal axis of subtidal depth-averaged velocities with ellipses centered at each mooring location. Mean absolute error ($\frac{1}{n}\sum_{i=1}^{n}|o_i - m_i|$, where n is the number of moorings, o is the observed variable, and m is the modeled variable) is 0.01m s^{-1} for u_{maj}, 0.02m s^{-1} for u_{min}, and 8.65° for the inclination.

	u_{maj} (m s^{-1})		u_{min} (m s^{-1})		Inclination (°)	
	Obs	Mod	Obs	Mod	Obs	Mod
MS100	0.079	0.122	0.044	0.036	101.7	98.1
NRL50N	0.088	0.111	0.044	0.031	79.0	91.9
NRL50S	0.114	0.107	0.038	0.024	115.8	93.8
OC40S	0.082	0.077	0.043	0.020	89.6	87.2
OC50	0.077	0.081	0.041	0.023	85.5	94.2
PS30M	0.090	0.121	0.038	0.016	82.8	85.6
PS30S	0.129	0.131	0.044	0.025	98.6	97.5
PS40S	0.112	0.120	0.050	0.026	101.5	96.7
PS40N	0.105	0.103	0.050	0.024	90.2	89.1
PS40M	0.114	0.119	0.046	0.024	104.1	94.5
PS50	0.096	0.119	0.045	0.025	87.8	94.4
VB30N	0.113	0.120	0.047	0.031	114.0	102.3
VB30S	0.104	0.096	0.032	0.016	122.6	97.5
VB50N	0.102	0.126	0.046	0.030	106.5	98.0

Table 3.2: Observed and modeled standard deviation for major axis barotropic velocities, standard deviation for minor axis barotropic velocities, phase (referenced to the equilibrium phase along Greenwich meridian as [*Pawlowicz et al.*, 2002]), and ellipse inclination (orientation in degrees counterclockwise positive from east). Statistics calculated from the M_2 barotropic velocities with ellipses centered at each mooring location. Mean absolute error ($\frac{1}{n}\sum_{i=1}^{n}|o_i - m_i|$, where n is the number of moorings, o is the observed variable, and m is the modeled variable) is 0.0045m s^{-1} for u_{maj}, 0.0049m s^{-1} for u_{min}, 10.70° for the phase, and 17.37° for the inclination.

	u_{maj} (m s^{-1})		u_{min} (m s^{-1})		Phase (°)		Inclination (°)	
	Obs	Mod	Obs	Mod	Obs	Mod	Obs	Mod
MS100	0.032	0.032	0.019	0.006	105.7	172.0	40.6	107.4
NRL50N	0.039	0.032	-0.005	0.006	152.5	152.9	87.0	85.4
NRL50S	0.055	0.055	-0.001	0.001	147.7	151.8	114.6	93.5
OC40S	0.025	0.026	0.010	0.006	159.4	163.5	118.3	83.0
OC50	0.029	0.026	0.002	0.008	161.6	157.0	111.2	88.2
PS30M	0.034	0.054	0.007	0.002	131.6	158.5	78.2	85.7
PS30S	0.047	0.053	0.015	0.006	159.1	166.6	94.8	102.2
PS40S	0.045	0.049	0.009	0.008	164.6	162.5	105.1	101.2
PS40N	0.034	0.041	0.006	0.006	151.0	160.8	98.3	87.0
PS40M	0.045	0.048	0.003	0.006	163.3	162.2	105.7	96.9
PS50	0.047	0.039	0.001	0.007	150.0	159.6	86.9	95.1
VB30N	0.045	0.049	0.011	0.008	174.3	168.0	121.0	112.9
VB30S	0.042	0.040	0.009	0.007	155.1	151.8	126.8	92.3
VB50N	0.051	0.049	0.011	0.009	159.6	163.8	102.0	107.7

The major axis tidal velocities are close in magnitude between observations and model, and there is an overall trend in major axis velocities decreasing from south to north. However, more variation between the observations and model exists in the minor axis velocities, and this variability is also seen in the ellipticity. The phase in the model agrees with the observations. In general, the orientations of the major axes of the tidal velocity ellipses tend to follow the bathymetry contours in the observations and model, but there are a few locations where the model does not capture the inclination well.

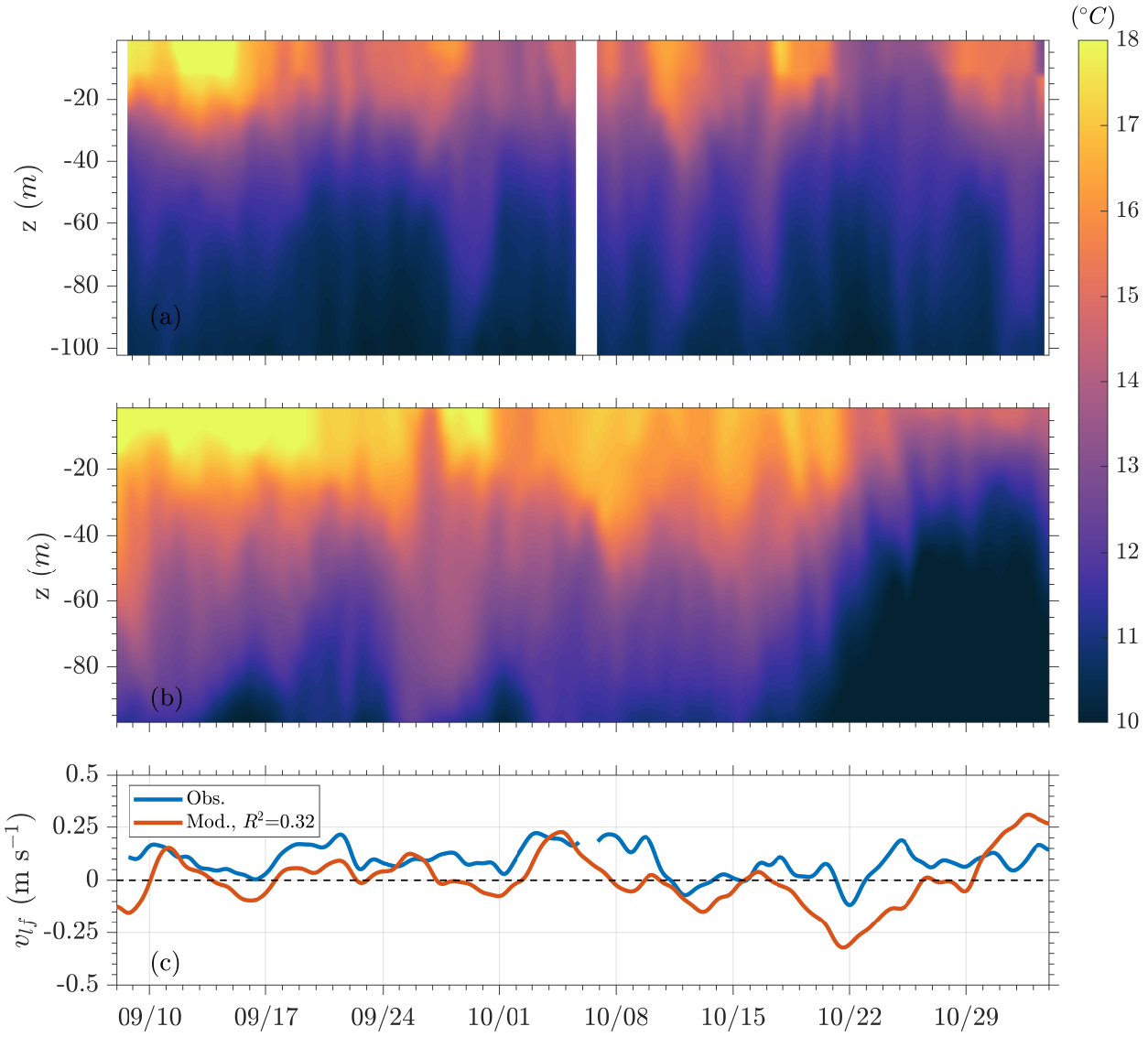

Figure 3.2: Observed (a) vs. modeled (b) lowpass-filtered (period > 33hrs) temperature. Panel (c) indicates the observed (blue) vs. modeled (red) north-south component of depth-averaged lowpass-filtered velocities at **MS100**.

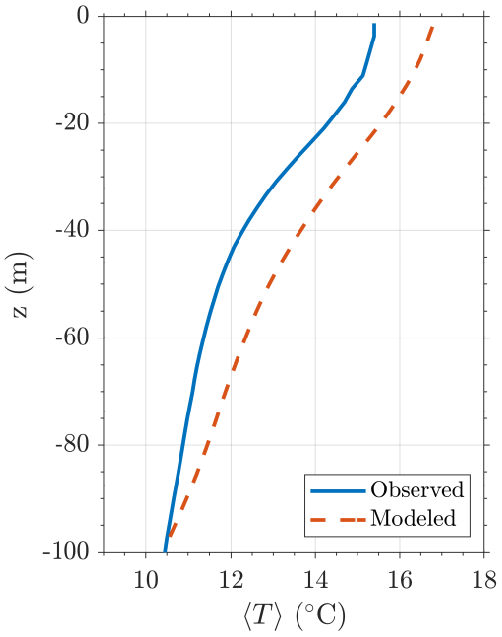

Figure 3.3: Observed (blue solid line) vs. modeled (red dashed line) time-averaged temperature vs. depth at **MS100**.

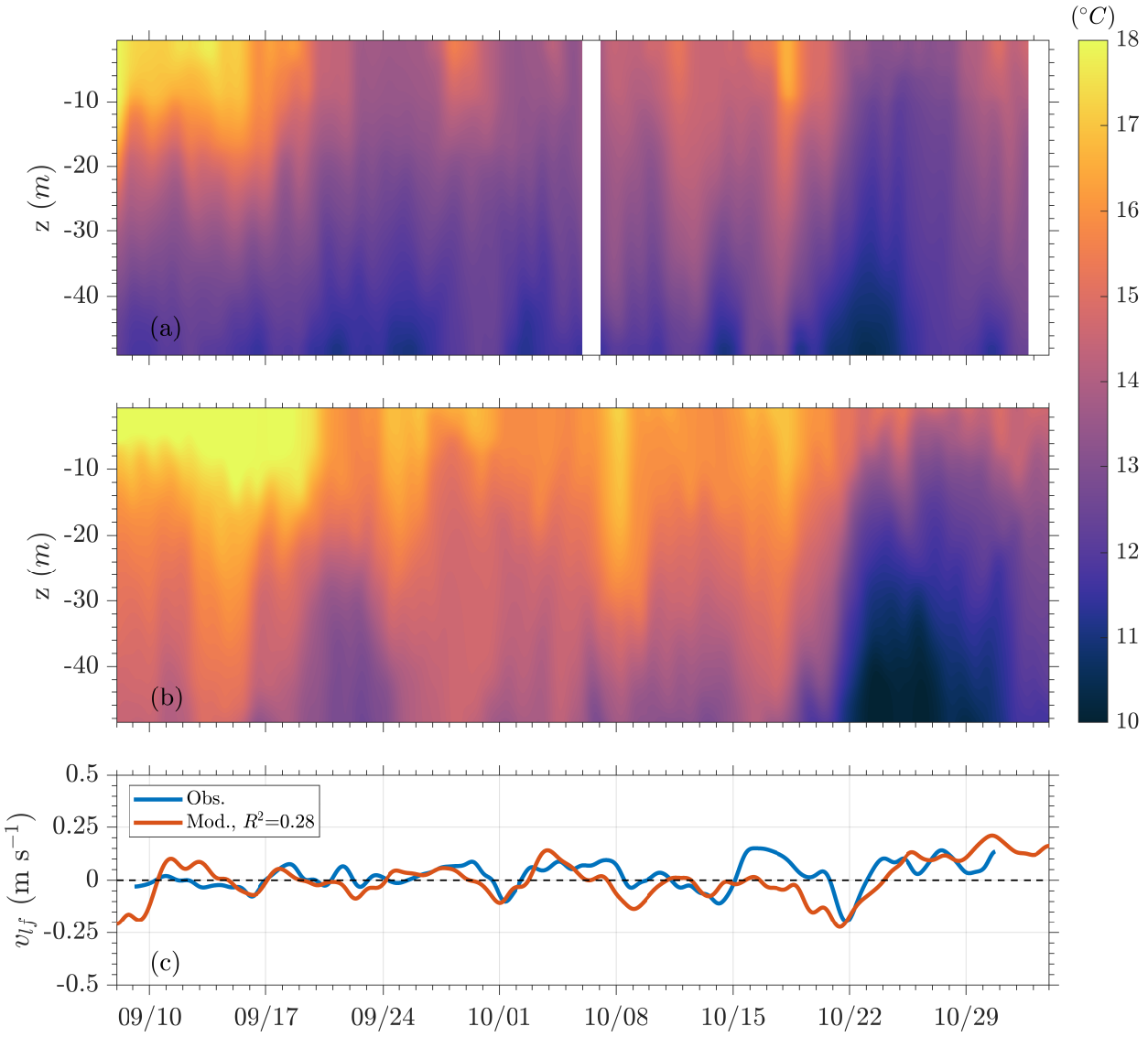

Figure 3.4: Observed (a) vs. modeled (b) lowpass-filtered (period >33 hrs) temperature. Panel (c) indicates the observed (blue) vs. modeled (red) north-south component of depth-averaged lowpass-filtered velocities at **OC50**.

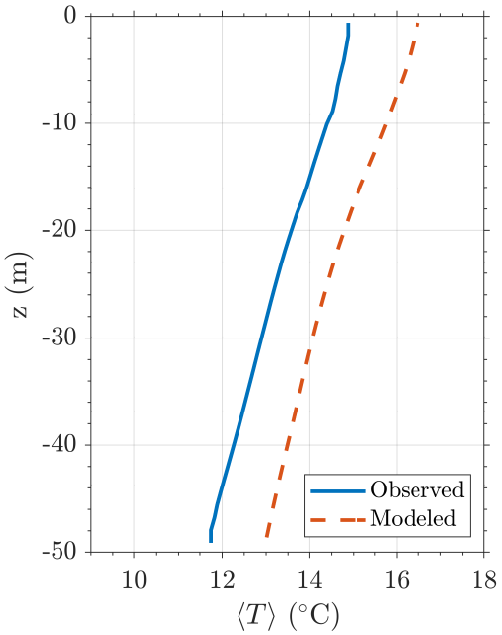

Figure 3.5: Observed (blue solid line) vs. modeled (red dashed line) time-averaged temperature vs. depth at **OC50**.

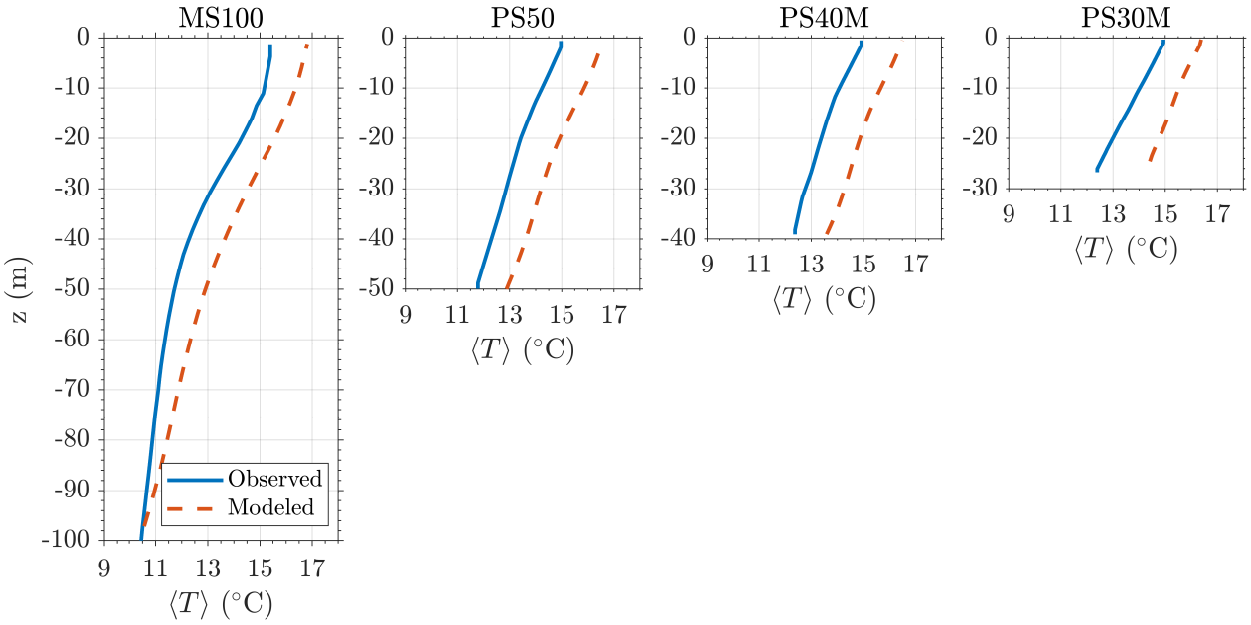

Figure 3.6: Cross-shore variation of Observed (blue solid line) vs. modeled (red dashed line) time-averaged temperature vs. depth at four different locations from 100 to 30 m depth (**MS100**, **PS50**, **PS40M**, and **PS30S**).

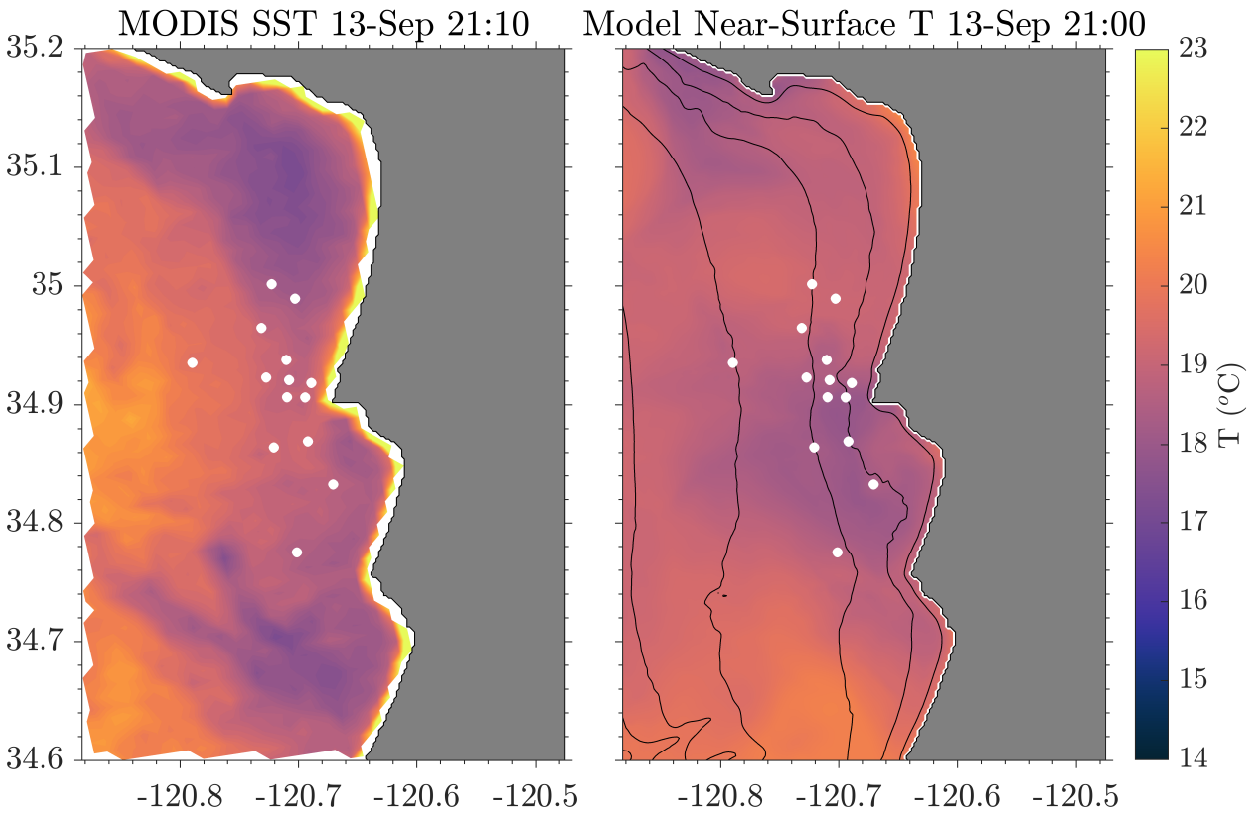

Figure 3.7: Snapshot of observed MODIS SST (left) vs. modeled near-surface temperature (right) from 13-Sep-2017. White dots indicate mooring locations.

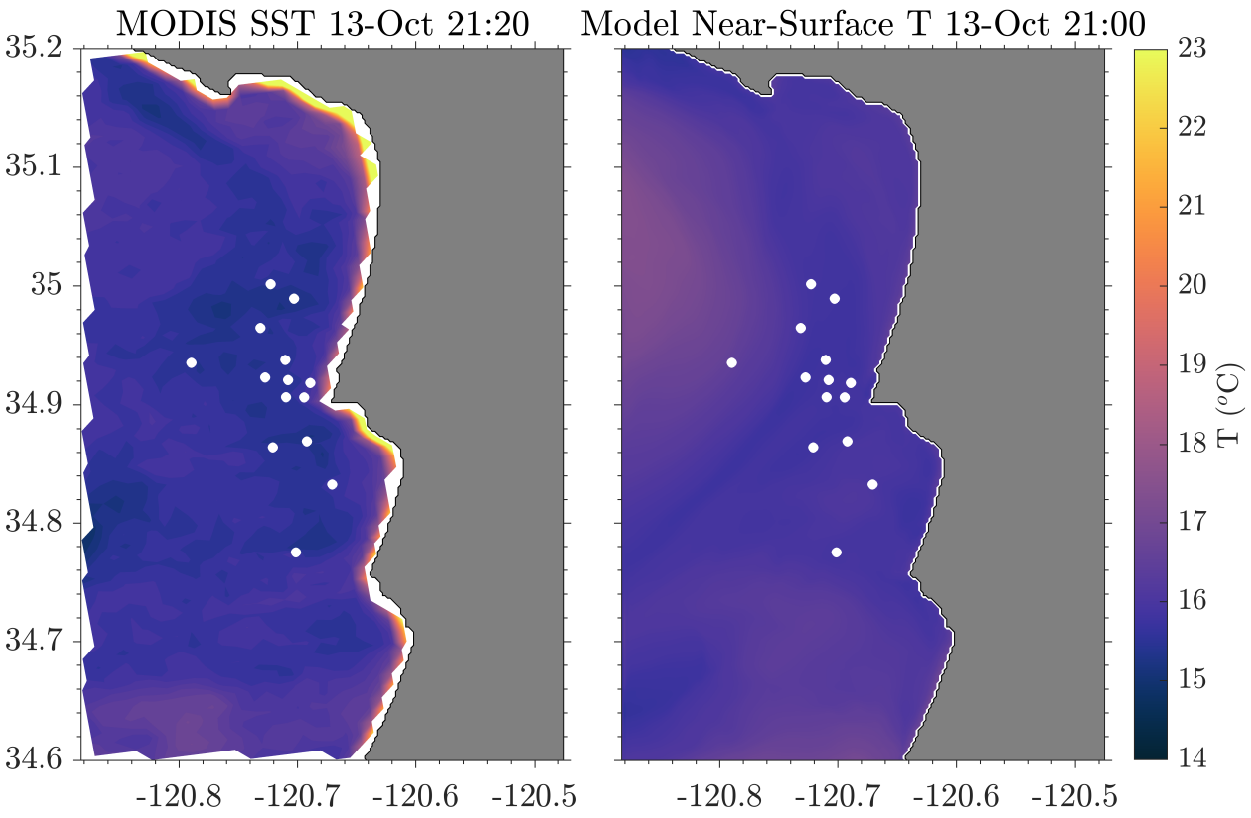

Figure 3.8: Snapshot of observed MODIS SST (left) vs. modeled near-surface temperature (right) from 13-Oct-2017. White dots indicate mooring locations.

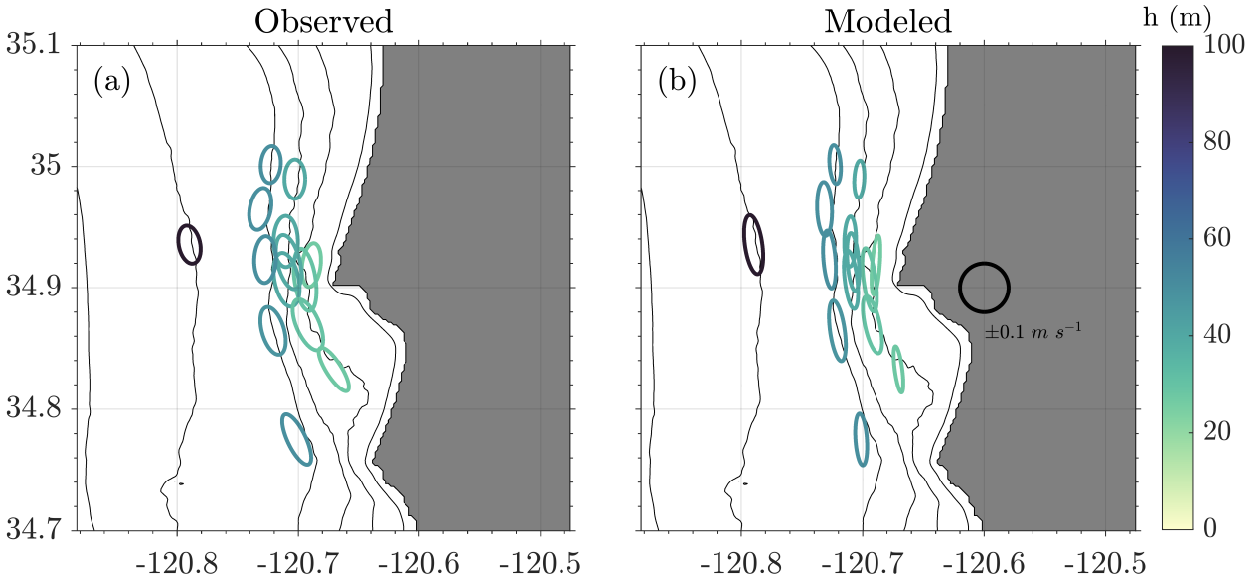

Figure 3.9: Observed (left) vs. modeled (right) principal axis of subtidal depth-averaged velocities with ellipses centered at mooring locations.

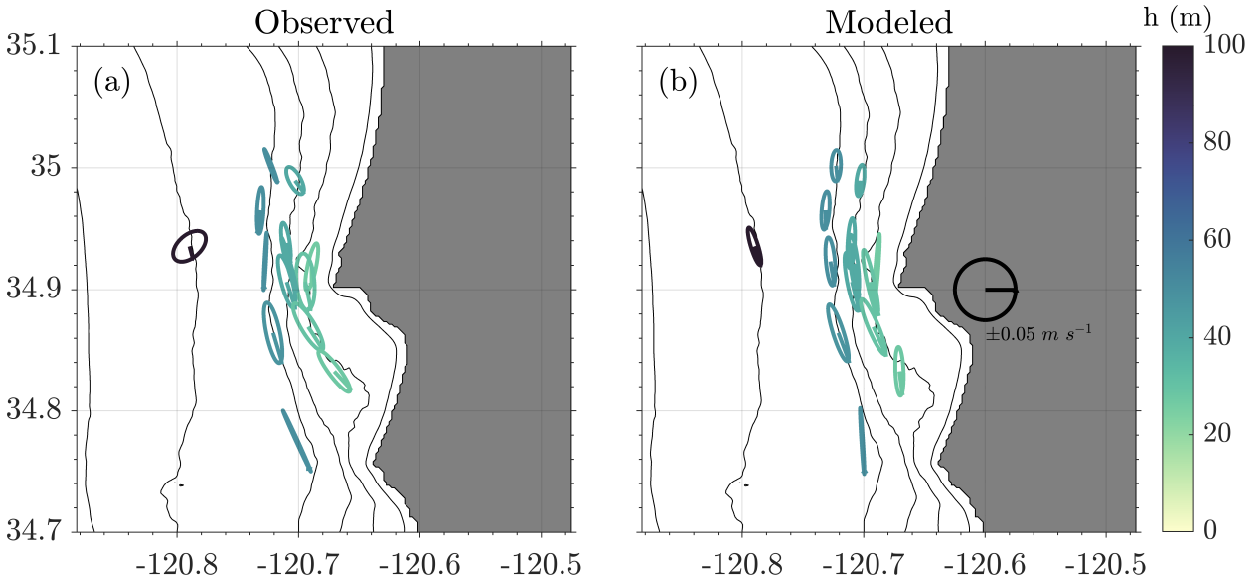

Figure 3.10: Observed (left) vs. modeled (right) principal axis of barotropic tidal velocities (for M_2) with ellipses centered at mooring locations.

Chapter 4

INTERNAL TIDAL DYNAMICS

Observed and modeled internal tidal dynamics in the shelf have only been considered for a cross-shelf transect. Synoptic variability in internal tidal property on length scales of ∼25 km are not considered previously and are discussed using a combination of modeled and observed dynamics. Since the model does fairly well capturing subtidal processes compared to observations on 50-km length scales, the baroclinic processes can be investigated.

4.1 Baroclinic Velocity and Pressure

Mode 1 internal tides have fast group speeds and have high energy density and, therefore, are responsible for most of the internal tidal energy fluxes. Internal tides often have a mode 1 structure [e.g., *Sherwin*, 1988], but higher mode internal waves have been observed on the continental shelf [e.g., *Shroyer et al.*, 2010]. Mechanisms for higher mode internal waves forming have been attributed to nonlinear instabilities due to shoaling [*Helfrich and Melville*, 1986] or a mode 1 wave interacting with a sill [e.g., *Hüttemann and Hutter*, 2001; *Vlasenko and Hutter*, 2001].

An example of modeled and observed u' and p' during a brief period two-day period is shown in Figure 4.1. During this time period for both the observations and the model, there is higher modal variability in the baroclinic velocities than in the baroclinic pressure which exhibits a stronger mode 1 signal. Velocity measurements had a higher vertical resolution than for temperature, which could lead to the observational sensors not resolving higher modes in the pressure signal.

Averaged across all moorings, the observed baroclinic velocities (Figure 4.2) are composed of ∼65% mode 1 signal, ∼25% mode 2, and ∼10% mode 3. The modeled u' (Figure 4.2) are

composed of ∼60% mode 1 signal, ∼25% mode 2, and ∼15% mode 3.

For p' (Figure 4.2), the observations are made up of ∼80% mode 1 signal, ∼15% mode 2, and ∼5% mode 3. The modeled p' is made up of ∼75% mode 1 signal, ∼20% mode 2, and ∼5% mode 3. For both u' and p', the observations are characterized by slightly stronger mode 1 signal than what is seen in the model (by ∼5–10%), which shows more higher modal variability.

4.2 Temporal Variability of Baroclinic Energy Fluxes

Observed and modeled internal tidal energy fluxes (**F**) are considered at the mooring **OC50** (i.e., the northernmost mooring along the 50 m isobath, Figure 2.1). Observed energy fluxes are strongest in the u-direction (up to 70 W m^{-1}), indicative of primarily eastward propagation of internal tides. The v-component of observed internal tidal energy flux is usually ± 20 W m^{-1} with a negligible mean. For the model, the dominant component of baroclinic energy fluxes is in the u-direction with an onshore-directed propagation of energy as seen in the observations, but the v-direction with a more southward orientation for the direction of fluxes. The model predominantly underestimates the u- and v-component of baroclinic energy fluxes; however, the peak of baroclinic energy fluxes in the east-west direction—at ∼75 W m^{-1}—is a similar magnitude to those observed. For the v-component of the energy fluxes, the fluxes are in general underestimated with the exception of a peak magnitude of ∼35 W m^{-1}, which is in the opposite direction as the observations. The underestimation of modeled fluxes can be attributed to a lack of remotely-generated baroclinic energy and that the model simulations did not include data assimilation.

Overall, the model predicts larger magnitudes of internal energy fluxes in second deployment period. The largest magnitudes of modeled baroclinic energy fluxes coincides with the prolonged upwelling-favorable wind event that began around October 21. This may be due to increased or prolonged stratification in the model that was not seen in observations. The mean energy flux during deployment 1 is 22.8 W m^{-1} for the observations and 9.7 W m^{-1} while in deployment 2 these values are 24.2 W m^{-1} and 24.0 W m^{-1}, respectively.

4.3 Spatial Variability of Baroclinic Energy Fluxes

Measurements on a length scale of ∼10 km in the cross-shelf and ∼25 km in the alongshelf allows for identifying spatial variability of baroclinic energy flux.

Mean magnitudes of observed energy fluxes vary from 140.2 to 2.6 W m^{-1} (Figure 4.4), predominantly directed to the east-south-east except at the deepest location (**MS100**) and locations adjacent to Point Purisima (east-north-east) and Oceano (due east). The fluxes are strongest at the **MS100** mooring and decrease farther onshore, indicative of internal tidal energy dissipation. Furthermore, strong fluxes are observed adjacent to Point Sal and decrease at locations north and south of this headland.

The mean magnitudes of modeled energy fluxes vary from 81.2 to 3.2 W m^{-1} (Figure 4.4) and are predominantly directed to the east-south-east (as in the observations) except **MS100** which is directed slightly south of due east. The time-averaged baroclinic energy fluxes for the deployment period indicate that the mean baroclinic energy fluxes are larger in magnitude in the observations than in the model, the modeled fluxes are strongest at **MS100** and decreasing farther onshore, and strong fluxes adjacent to Point Sal decrease north and south of Point Sal.

Consistent between the observations and model are the variations in both the cross-shelf and alongshelf directions. At most mooring locations, the mean direction in the observations and model correspond well at most locations. The model poorly captures the direction of the fluxes at the moorings farthest from Point Sal—the farthest offshore, northernmost, and southernmost (**MS100**, **OC50**, **NRL50S**, respectively). There is also a strong cross-shelf gradient (Figure 4.5) as the strongest baroclinic energy fluxes are offshore and decrease closer to the shore as dissipation occurs. The cross-shelf dissipation occurs more quickly in the observations than the model and has an e-folding scale of roughly 2.3 km vs. 2.7 km. This length-scale of dissipation is consistent with previous observations (2–2.4 km, *Colosi et al.*, 2018).

Table 4.1: Observed and modeled baroclinic energy fluxes in the u- and v-direction (F_u and F_v, respectively) and the angle of the direction of the mean flux vector ($\mathbf{F} = \sqrt{F_u^2 + F_v^2}$) in degrees counterclockwise positive from east. Mean absolute error ($\frac{1}{n}\sum_{i=1}^{n}|o_i - m_i|$, where n is the number of moorings, o is the observed variable, and m is the modeled variable) is 10.00 W m^{-1} for F_u, 3.99 W m^{-1} for u_{min}, and 8.60° for the inclination.

	F_u (W m^{-1})		F_v (W m^{-1})		Inclination (°)	
	Obs	Mod	Obs	Mod	Obs	Mod
MS100	135.63	79.09	11.21	-2.75	4.73	-1.99
NRL50N	34.8	26	-8.95	-6.37	-14.42	-13.77
NRL50S	26.51	17.84	3.2	-4.7	6.89	-14.74
OC40S	13.83	9.49	0.63	-3.88	2.6	-22.26
OC50	23.59	17.33	-1.78	-3.41	-4.31	-11.12
PS30M	2.22	2.6	-0.38	-1.47	-9.65	-29.6
PS30S	9.34	7.35	-3.7	-2.6	-21.63	-19.46
PS40S	22.3	17.07	-9.3	-5.7	-22.64	-18.48
PS40N	21.29	14.67	-4.88	-5.32	-12.91	-19.91
PS40M	15.13	14.66	-7.28	-5.49	-25.7	-20.54
PS50	49.09	29.38	-16.27	-9.69	-18.34	-18.24
VB30N	8.83	6.6	-2.71	-2.14	-17.05	-17.96
VB30S	6.34	3.7	1.22	-0.17	10.88	-2.65
VB50N	45.08	29	-14.36	-5.59	-17.67	-10.9

4.4 Spatial Variability of APE & HKE

The behavior of freely-propagating waves greatly differ from standing waves, which are formed from the superposition of two progressive waves travelling in opposite directions. Determining the difference between progressive and standing waves as fluxes from standing waves can be misleading for identifying sources of internal waves. Additionally, circulation and material exchange from a standing internal wave is different than from progressive internal waves.

The ratio of available potential energy (APE) to horizontal kinetic energy (HKE) for the observations and model outputs (Figure 4.6) is indicative of standing vs. progressive nature of internal waves and can be diagnosed as a function of frequency. The ratio of a progressive wave for the semidiurnal (M_2) frequency is indicated by

$$\frac{APE}{HKE} = \frac{\omega^2 - f^2}{\omega^2 + f^2}$$

which is roughly equal to 0.4769 at the latitude of Point Sal (34.9°N). If the ratio of APE to HKE is above this value, the internal tide is no longer considered a propagating wave. The ratio of a wave where rotation is no longer important is 1-to-1 (as $f \to 0$, $\frac{\omega^2 - f^2}{\omega^2 + f^2} \to \frac{\omega^2}{\omega^2} = 1$). Values for APE and HKE exhibit bulk behavior as they were integrated over a band from 1–16 hours not just the M_2 frequency. In the observations, the ratio of APE to HKE in deeper waters is indicative of a progressive wave at the M_2 tidal frequency. In the model, the ratio of APE to HKE in deeper waters is between a progressive and a standing wave, but in shallower waters is indicative of a standing wave. The ratio of APE to HKE is just one method to investigate the progressive vs. standing nature of internal waves and additional analysis will further investigate these dynamics.

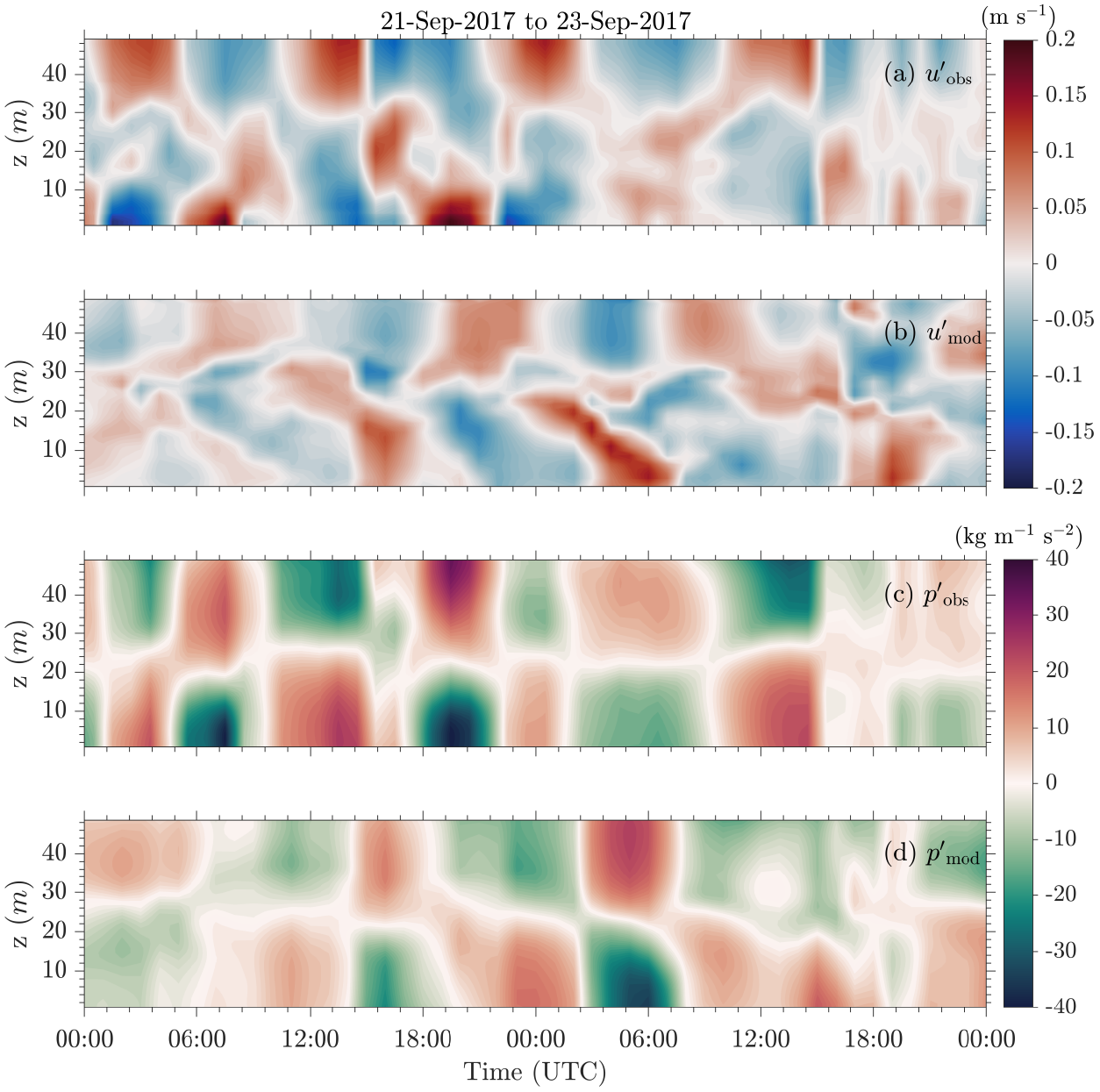

Figure 4.1: Example baroclinic velocity and pressure profiles vs. time

Observed (a) and modeled (b) baroclinic u-velocity perturbation and the observed (c) and modeled (d) baroclinic pressure perturbation at **OC50** from September 21–23, 2017. Baroclinic energy fluxes were of a similar magnitude during this time.

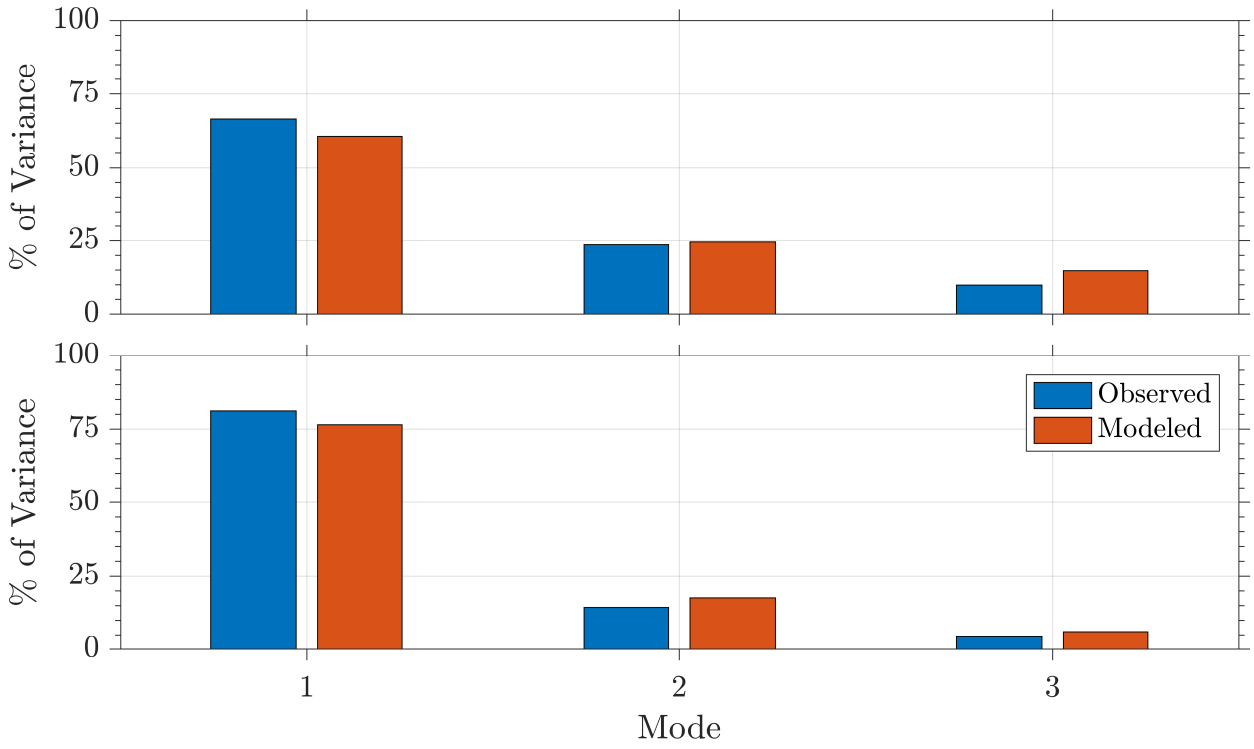

Figure 4.2: Observed (blue) vs. modeled (red) percent variance described by modes 1, 2, and 3 from a modal decomposition of baroclinic velocity u' (top) and pressure p' (bottom) perturbations averaged across all moorings.

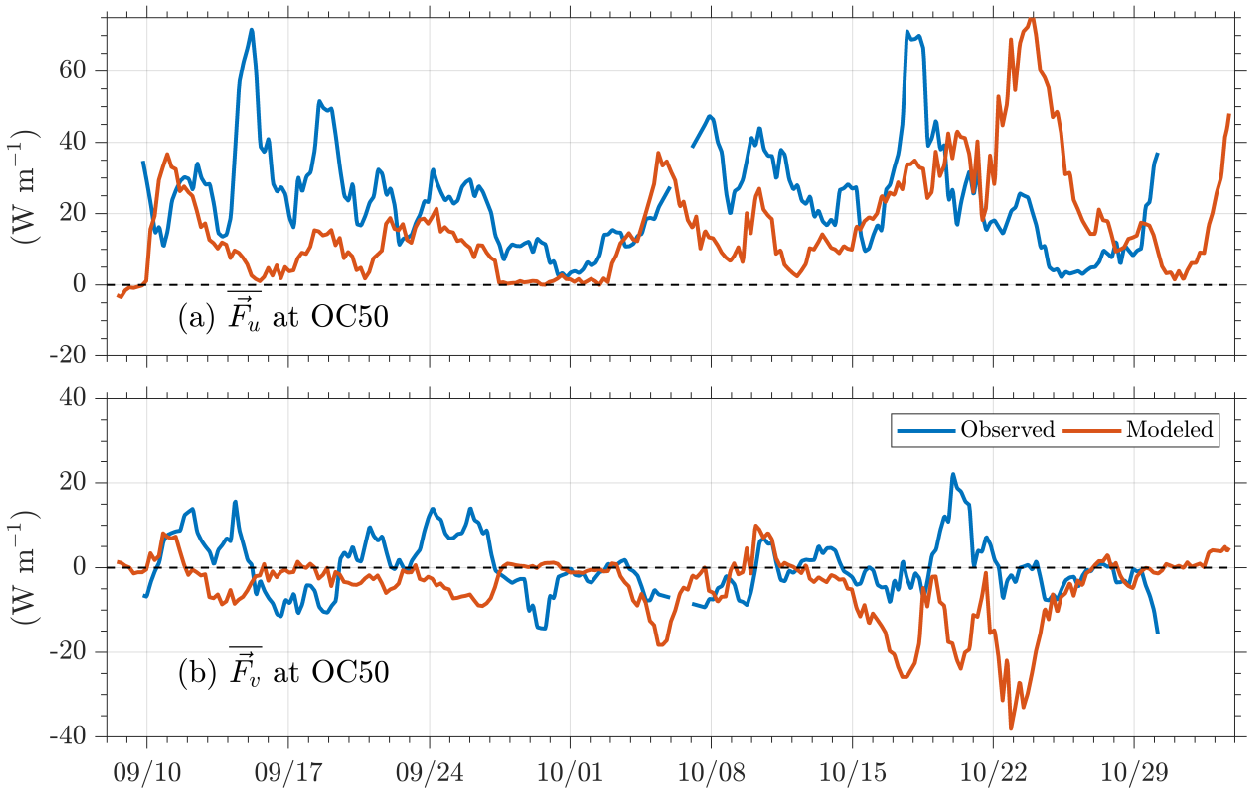

Figure 4.3: Observed (blue) vs. modeled (red) baroclinic energy fluxes for the east-west (top) and north-south (bottom) components at **OC50**.

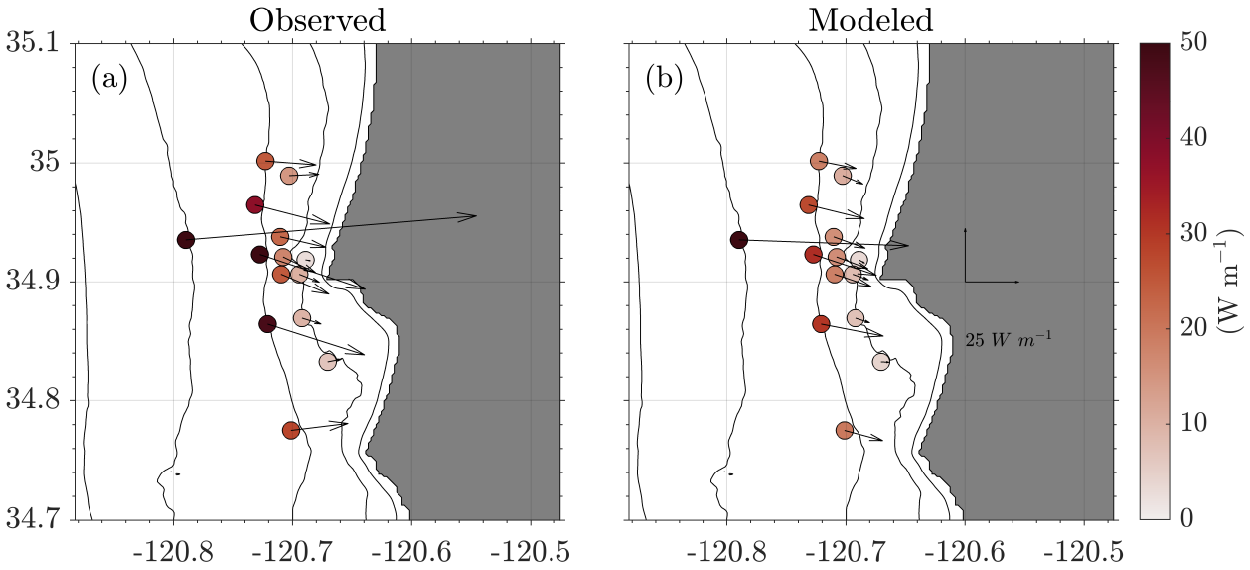

Figure 4.4: Observed (left) vs. modeled (right) baroclinic energy fluxes (time-averaged over the deployment period). Each dot represents the location of each mooring used in the analysis, and is color-coded by the time-averaged magnitude of baroclinic energy fluxes. Black vectors indicate mean magnitude and direction at each location.

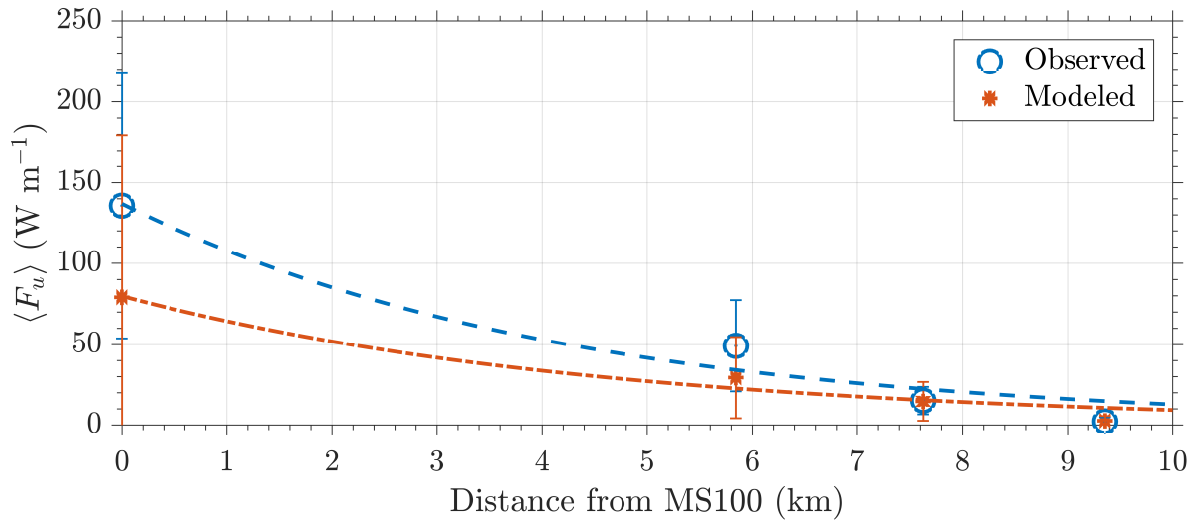

Figure 4.5: Observed (blue circle) vs. modeled (red star) time-averaged baroclinic energy fluxes (F_u) at each mooring in a cross-shelf transect off Point Sal (moorings **MS100**, **PS50**, **PS40M**, **PS30M**) plotted against the distance from the farthest offshore mooring, **MS100**. Mean fluxes are plotted with an exponential decay fit for the observations (blue) and model (red). Error bars represent the standard deviation of the fluxes.

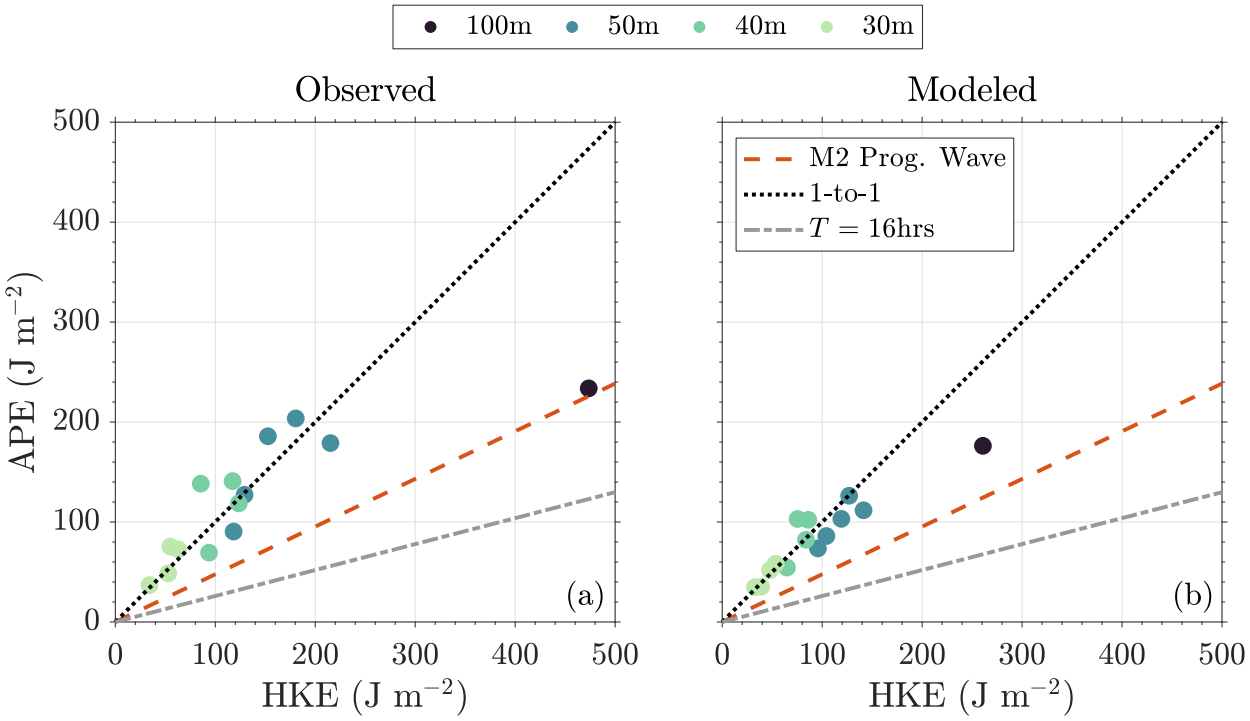

Figure 4.6: Observed (left) vs. modeled (right) scatter of time-averaged APE to HKE. Dots are colored by isobath. The red dashed line indicates the ratio of a progressive wave at Pt. Sal (rotation important), and the black dotted line indicates a 1-to-1 correspondence in the ratio (rotation not important).

Chapter 5

DISCUSSION

The SMB is a dynamic region with many physical processes driving circulation and stratification, and local changes in stratification could alter the propagation of internal tides in the region. For instance, enhanced upwelling to the lee side of the headland [*Gan and Allen*, 2002] at Point Sal may contribute to alongshelf variability of stratification and can impact the propagation of internal tides [e.g., *Kurapov et al.*, 2010]. Also, changes in stratification from wind-relaxation events and eddy shedding processes from the shoreline variability may affect local internal tidal dynamics. Here, the alongshelf variability in internal tides and processes driving it are investigated. Also, the progressive vs. standing nature of the internal tidal signal is discussed further.

5.1 Alongshelf Variability

The time mean baroclinic energy fluxes (Figure 4.4) indicate variability in the alongshelf direction to the north and south of Point Sal in both the observations and model. To investigate the alongshelf variability along the 50 m isobath, a time series of baroclinic energy fluxes comparing the northernmost and southernmost moorings on the 50 m isobath (**OC50** and **NRL50S**, respectively) is considered (Figure 5.1). Correlations between **OC50** and subsequent mooring on the 50 m isobath to the south for baroclinic energy fluxes and HKE are shown in Table 5.1.

Generally, the baroclinic energy flux correlation between **OC50** and **NRL50S** is poor for both observations ($R^2 = 0.11$) and the model ($R^2 = 0.05$). This difference over a length scale may occur due to variation in local stratification, which controls the local phase speed.

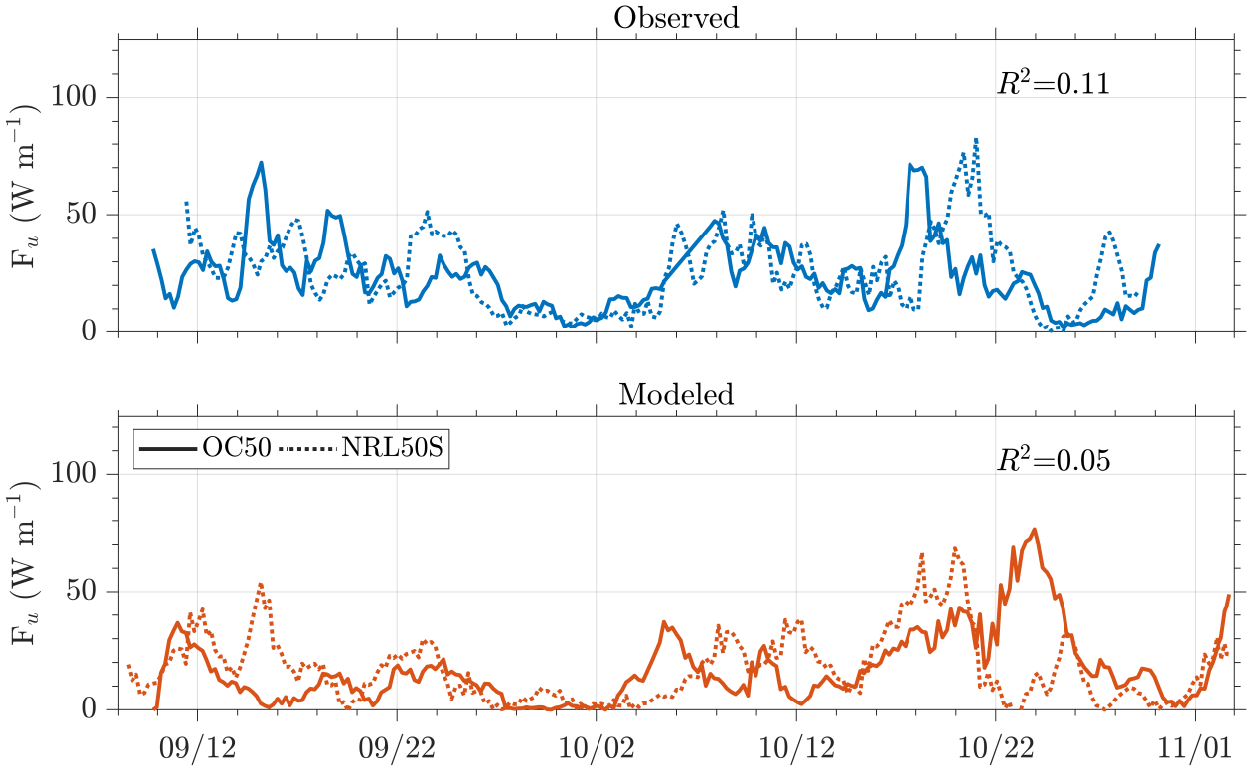

Figure 5.1: Observed (top) and modeled (bottom) baroclinic energy fluxes of the northernmost (**OC50**, solid line) and southernmost (**NRL50S**, dotted line) locations of moorings on the 50 m isobath.

5.1.1 Offshore Variability in Model Fluxes

Alongshore differences in baroclinic energy fluxes closer to shore could be, at least in part, attributed to differences in the fluxes farther offshore. Differences in internal tidal energy fluxes in 100 m of water could be due to factors such as multiple generation regions offshore and local generation in submarine canyons.

While there are no moored observations in deeper waters to investigate alongshelf variability in deeper waters, the numerical model allows us to investigate the alongshelf variability farther offshore. To do this, two locations representing hypothetical mooring locations in the model were chosen along the 100 m isobath at the same latitude as the moorings in the comparison along the 50 m isobath. The baroclinic energy fluxes from these hypothetical

Table 5.1: R^2 values for calculated baroclinic energy quantities (fluxes and HKE) between the observations and model. Correlation values are from the northernmost mooring (**OC50**) to each subsequent mooring from north to south along the 50 m isobath.

	Lat ($^\circ N$)	F_u		HKE	
OC50 to		Obs	Mod	Obs	Mod
OC50	35	1	1	1	1
NRL50N	34.96	0.55	0.7	0.58	0.64
PS50	34.92	0.29	0.33	0.21	0.38
VB50N	34.86	0.34	0.17	0.12	0.28
NRL50S	34.78	0.12	0.05	0.04	0.11

moorings on the 100 m isobath in the model (Figure 5.2) indicate alongshelf variability in the magnitude of baroclinic energy fluxes (peak magnitude of 150 W m^{-1} at the northern location vs. 300 W m^{-1} at the southern location) is present in deeper waters as well; however, the modeled alongshelf fluxes are more highly correlated ($R^2 = 0.18$) at these depths. The decrease in alongshelf correlation in the model could be attributed to changes in local processes.

5.1.2 Alongshelf Stratification Variability

Alongshelf variability of the stratification (Figure 5.3) in the observations and the model is examined using the same locations along the 50 m isobath (**OC50** and **NRL50S**). Between these two locations, the observations are more strongly correlated ($R^2 = 0.59$) than in the model ($R^2 = 0.34$). Further investigation in the variability along the 50 m isobath (Table 5.2) indicates that the correlation from **OC50** to each subsequent mooring on the 50 m isobath decreases more rapidly in the model than the observations. Therefore, local processes in the model are contributing to additional alongshelf stratification variability not seen in the observations. For the depth-averaged major-axis velocities, however, the correlations

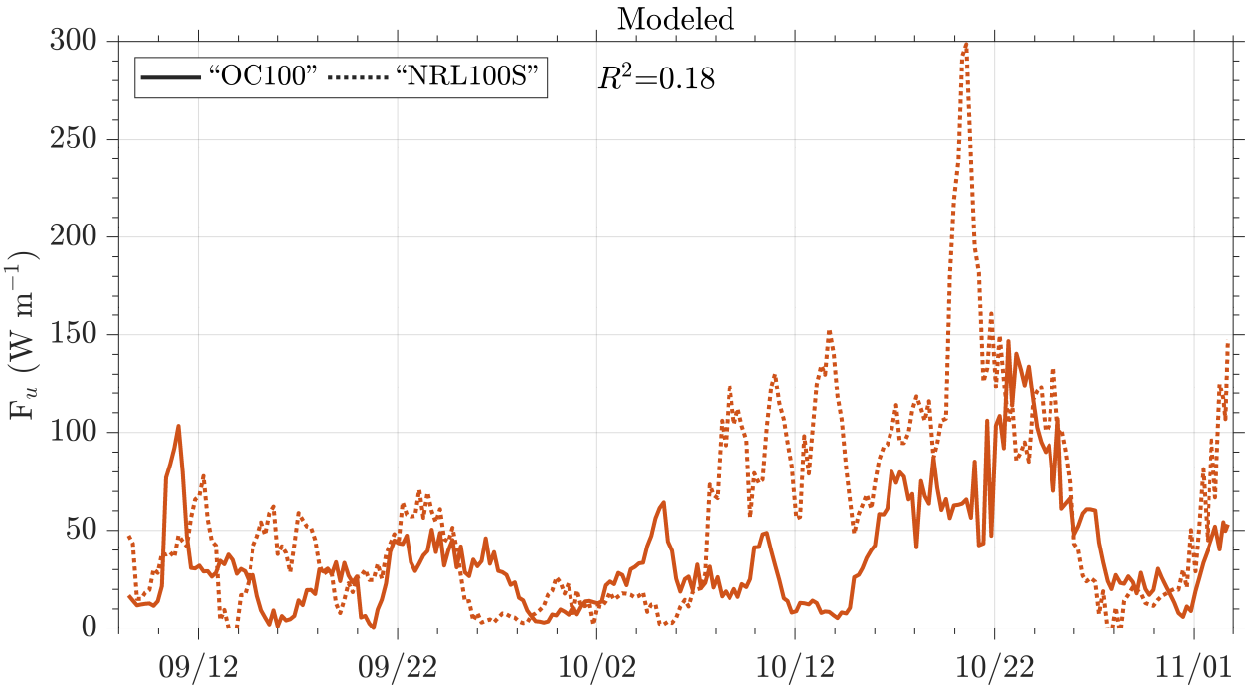

Figure 5.2: Modeled baroclinic energy fluxes of the northernmost and southernmost locations of hypothetical modeled moorings on the 100 m isobath that correspond in latitude with the moorings on the 50 m isobath. The mooring "OC100" corresponds to **OC50** but on the 100 m isobath (solid line), and "NRL100S" corresponds to **NRL50S** but on the 100 m isobath (dotted line).

decrease similarly between the observations and the model and are not contributing to the alongshelf difference in stratification.

5.1.3 Enstrophy Estimates

Another way to look at reasons for differences in stratification—and therefore baroclinic energy fluxes—is to look at the differences in eddy energy to the north and to the south of Point Sal. Differences in eddy activity could cause local changes in stratification and therefore alter the propagation of baroclinic energy fluxes. To quantify the vorticity, the

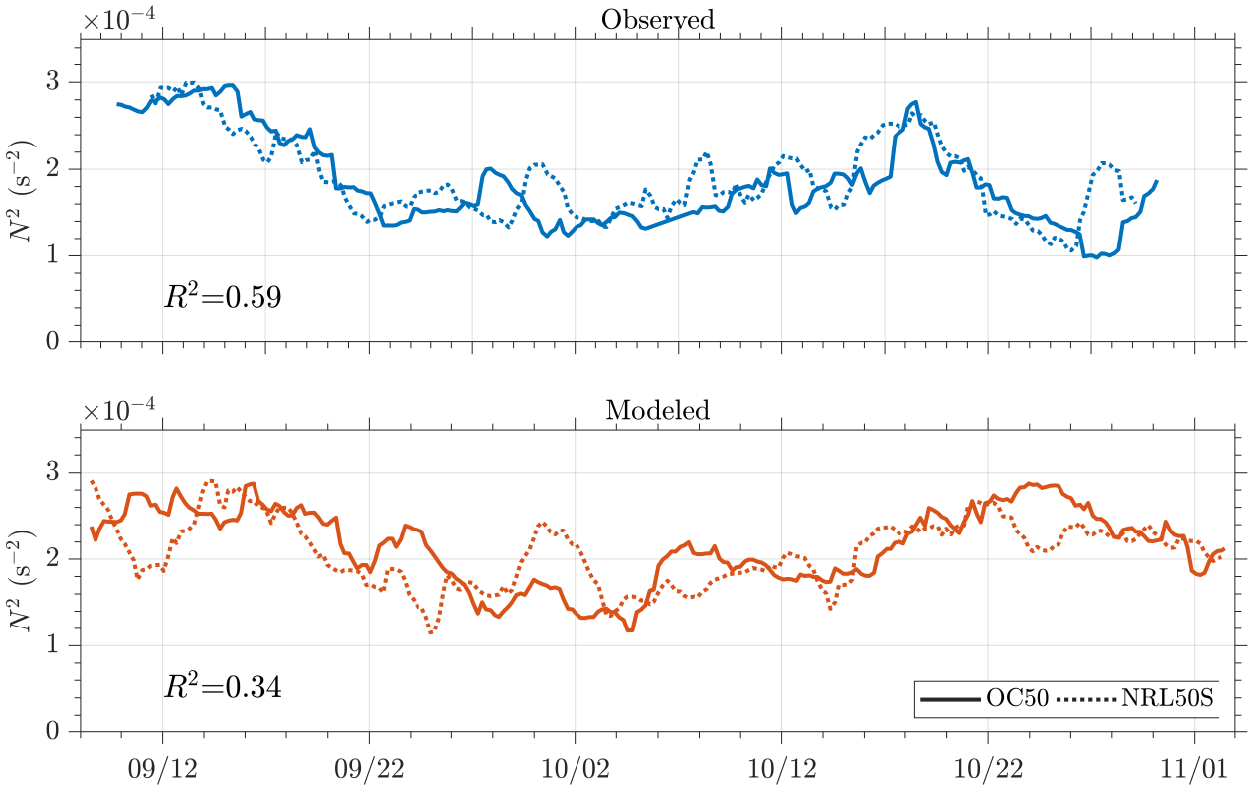

Figure 5.3: Observed (top) and modeled (bottom) depth-averaged stratification of the northernmost (**OC50**, solid line) and southernmost (**NRL50S**, dotted line) locations of moorings on the 50 m isobath.

measure of spatially-integrated enstrophy was calculated using

$$\frac{1}{L_x L_y} \int \int \xi^2 dx dy$$

where ξ is the modeled vorticity. The enstrophy was calculated in two regions in the model centered at the location of **OC50** and **NRL50S** with a radius of 2.5 km, which is slightly larger than the baroclinic Rossby radius

$$L_R = \frac{NH}{n\pi f_0}$$

in this region, where N is the Brunt-Väisälä frequency, H is the water depth, n is the mode (1 in this case), and f_0 is the Coriolis parameter $f_0 = 2\Omega \sin\theta$. The time series results of

Table 5.2: R^2 values for stratification (N^2) and subtidal-filtered depth-averaged velocities along the major and minor axes ($\bar{u}_{lf}$ and $\bar{v}_{lf}$, respectively) between the observations and model. Correlation values are from the northernmost mooring (**OC50**) to each subsequent mooring from north to south along the 50 m isobath.

	Lat ($^\circ N$)	N^2		$\bar{u}_{maj}$	
OC50 to		Obs	Mod	Obs	Mod
OC50	35	1	1	1	1
NRL50N	34.96	0.85	0.84	0.87	0.89
PS50	34.92	0.78	0.71	0.71	0.66
VB50N	34.86	0.74	0.60	0.43	0.41
NRL50S	34.78	0.59	0.35	0.28	0.3

the modeled enstrophy calculation from the regions to the north and to the south of the headland at Point Sal are shown in Figure 5.4. The decorrelation timescales—the number of hours for the signal to no longer be correlated with itself—of enstrophy differ from the regions to the north and to the south of the Point Sal (94 and 79 hours, respectively). There are clear differences in enstrophy between the two regions in the model indicating different eddy activity on opposite sides of the headland. Differences in eddy activity can alter local stratification thereby altering the propagation of internal tides.

5.2 Standing vs. Progressive Nature of Waves

5.2.1 Coherence and phase

Prior analysis into the standing vs. progressive nature in the SMB for both the observations and model were inconclusive (Section 4.4) and is investigated further. Examining the coherence and phase of internal tidal energy is another metric of estimating the nature of standing vs. progressive waves [e.g., *Lerczak et al.*, 2003; *Savidge et al.*, 2007; *Kumar et al.*, 2016].

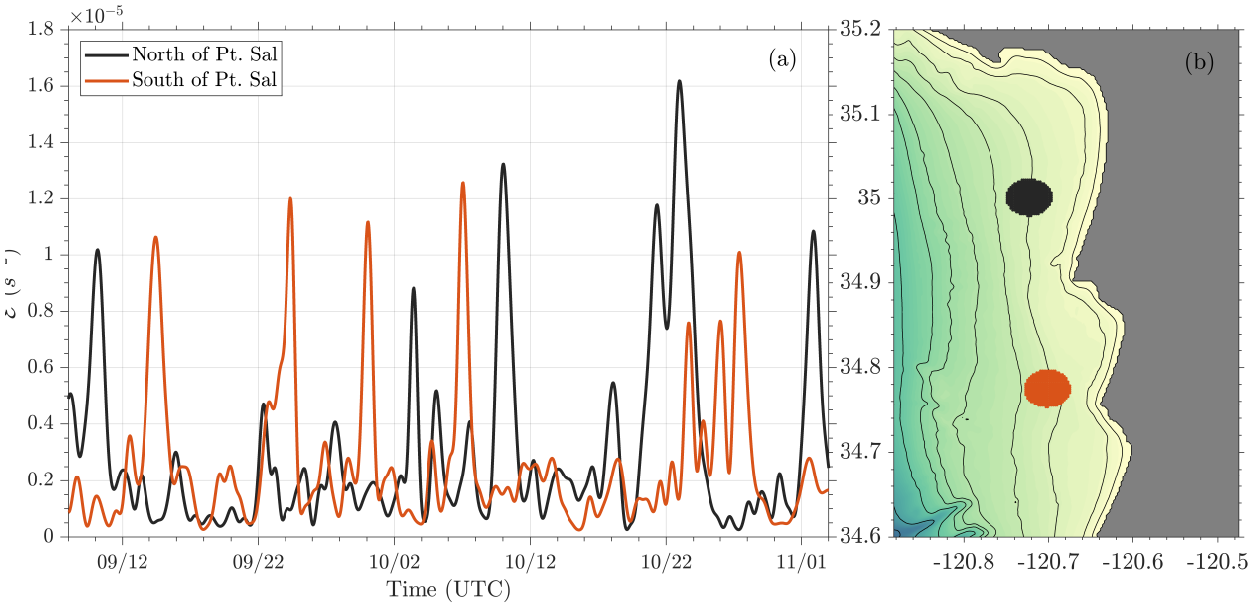

Figure 5.4: Spatially-integrated enstrophy (left) for a region north of Point Sal centered at **OC50** (black line) and south of Point Sal centered at (red line) calculated with $\frac{1}{L_x L_y}\int\int \xi^2 dxdy$ where ξ is the modeled vorticity. The regions with a radius of 2.5 km where the enstrophy is calculated is shown in the right panel. The decorrelation timescale is 94 hours at **OC50** and 79 hours at **NRL50S**.

The coherence $C_{u'p'}$ and phase $\Delta\theta_{u'p'}$ are calculated using cross-spectral analysis (Figures 5.5 and 5.6). The phase $\Delta\theta_{u'p'}$ can be used to differentiate between the progressive ($\Delta\theta_{u'p'} = 0°$) and standing ($\Delta\theta_{u'p'} = \pm 90°$) nature of mode-one internal tides as in *Lerczak et al.* [2003]. The 95% confidence intervals for error are calculated for coherence with

$$\delta_C = \frac{\sqrt{2}[1 - C_{u'p'}^2]^{0.5}}{|C_{u'p'}(\omega)|\sqrt{n_d}}$$

and for phase with

$$\delta_\theta = \frac{[1 - C_{u'p'}^2]^{0.5}}{|C_{u'p'}|\sqrt{2n_d}},$$

where n_d is the degrees of freedom [*Bendat and Piersol*, 2011].

At **MS100** (Figure 5.5), the observations are strongly coherent at the M_2 frequency in both deployments 1 and 2 ($C_{u'p'}^{obs} \approx 0.95$). The observed phase $\Delta\theta_{u'p'}^{obs} \approx -25°$ in deployment 1 indicating a mostly progressive wave, and $\Delta\theta_{u'p'}^{obs} \approx 0°$ in deployment 2 indicating that the

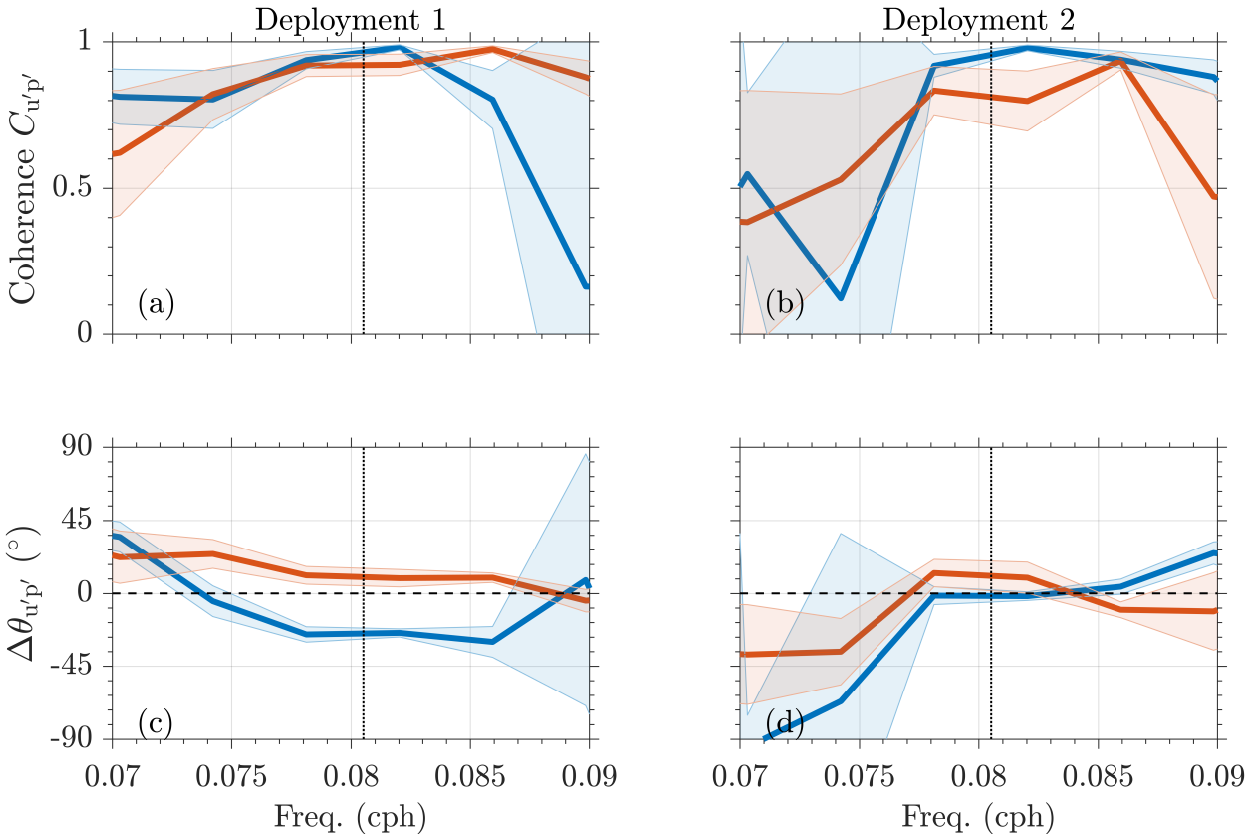

Figure 5.5: Observed (blue line) and modeled (red line) coherence $C_{u'p'}$ (top panels) and phase $\Delta\theta_{u'p'}$ (bottom panels) for deployment 1 (left) and deployment 2 (right) at **MS100**—the farthest offshore mooring location. Semidiurnal frequency of ~ 0.0805cph is indicated by the black dotted line.

internal tide is more strongly progressive during this time period. The model is strongly coherent at the M_2 frequency in deployment 1 ($C^{mod}_{u'p'} \approx 0.9$), and in deployment 2, the modeled coherence drops to 0.8. The modeled phase $\Delta\theta^{mod}_{u'p'} \approx 10°$ for both deployments 1 and 2, indicating a strongly progressive nature for both deployment periods.

At 50m water depth (**OC50**, Figure 5.6), the observations are strongly coherent at the M_2 frequency in both deployments 1 and 2 ($C^{obs}_{u'p'} \approx 0.95$) as in deeper waters. The observed phase $\Delta\theta^{obs}_{u'p'} \approx 5°$ in both deployment 1 and 2, indicating a strongly progressive nature for both deployment periods. The model is strongly coherent at the M_2 frequency in deployment

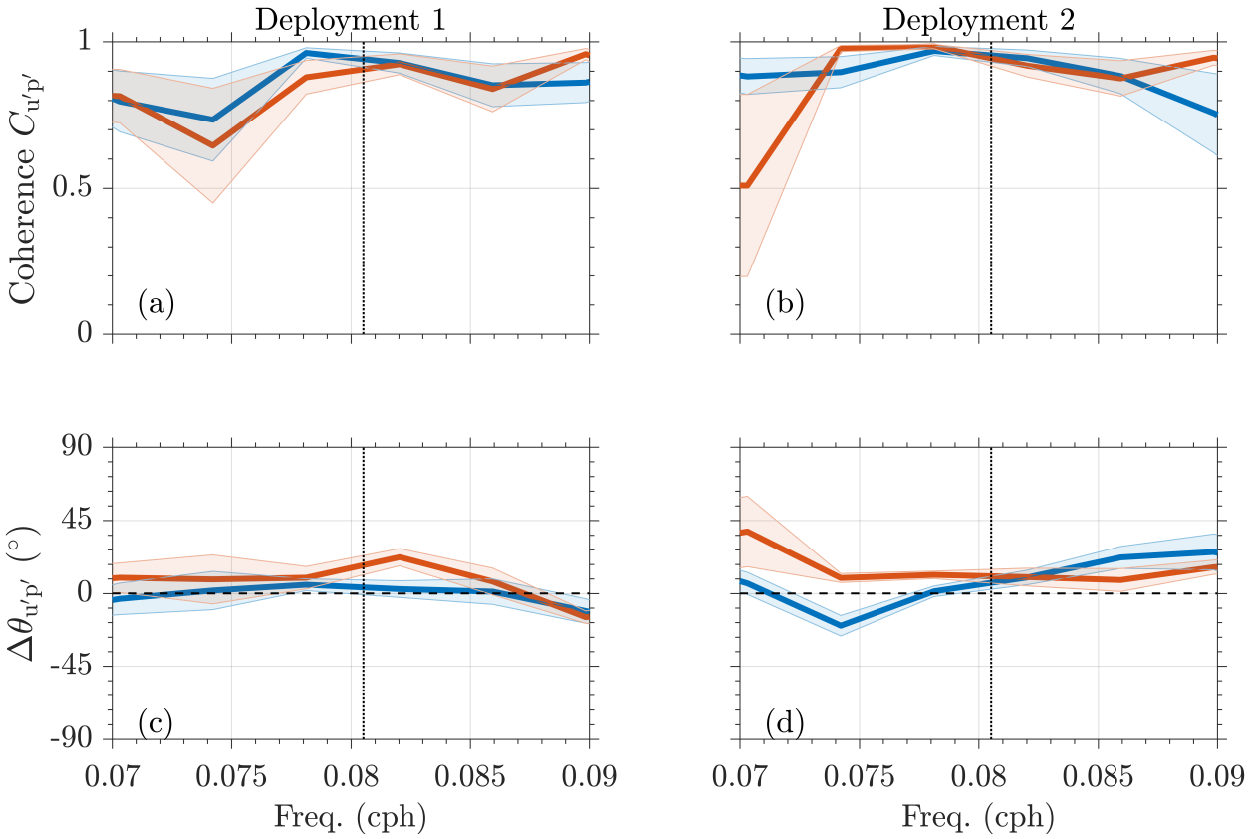

Figure 5.6: Observed (blue line) and modeled (red line) coherence $C_{u'p'}$ (top panels) and phase $\Delta\theta_{u'p'}$ (bottom panels) for deployment 1 (left) and deployment 2 (right) at **OC50**—the farthest north mooring location on the 50m isobath. Semidiurnal frequency of ∼0.0805 cph is indicated by the black dotted line.

1 ($C^{mod}_{u'p'} \approx 0.9$), and in deployment 2, the modeled coherence increases to 0.95. The modeled phase $\Delta\theta^{mod}_{u'p'} \approx 10°$ for deployment 1 and $\Delta\theta^{mod}_{u'p'} \approx 10°$ for deployment 2.

Cross-shelf velocity coherence $C_{u'u'}$ can be calculated using cross-spectral analysis between the baroclinic velocities between two moorings (Figures 5.7 and 5.8). The velocity coherence can be used to computed a wave speed

$$c = \frac{\Delta x}{\Delta T}$$

where $\Delta T = \frac{T_{M_2}\Delta\theta_{u'u'}}{360°}$. Similarly, the semidiurnal wave speed can be calculated using the cross-shelf change in phase ($\Delta\theta$) from the pressure coherence $C_{p'p'}$. Both speeds can be

Table 5.3: Table values of wave speeds from **MS100** to **PS50** calculated from phase ($c = \frac{\Delta x}{\Delta T}$, where $\Delta T = \Delta\theta\frac{12.42}{2\pi}$) and using the internal wave speed $c = \frac{Nh}{\pi}$, where N is calculated using the mean stratification plus and minus the standard deviation.

	MS100 to PS50			
	Deployment 1		Deployment 2	
	Obs	Mod	Obs	Mod
$\frac{\Delta x}{\Delta T}\|_{u'}$	0.47–0.57	0.48–0.60	0.37–0.55	0.46–0.53
$\frac{\Delta x}{\Delta T}\|_{p'}$	0.33–0.37	0.40–0.49	0.32–0.39	0.39–0.45
Nh/π	0.25–0.38	0.21–0.28	0.24–0.33	0.22–0.28

Table 5.4: Table values of wave speeds from **PS50** to **PS30M** calculated from phase ($c = \frac{\Delta x}{\Delta T}$, where $\Delta T = \Delta\theta\frac{12.42}{2\pi}$) and using the internal wave speed $c = \frac{Nh}{\pi}$, where N is calculated using the mean stratification plus and minus the standard deviation.

	PS50 to PS30M			
	Deployment 1		Deployment 2	
	Obs	Mod	Obs	Mod
$\frac{\Delta x}{\Delta T}\|_{u'}$	0.15–0.16	0.17–0.19	0.16–0.21	0.18–0.23
$\frac{\Delta x}{\Delta T}\|_{p'}$	0.16–0.18	0.17–0.19	0.19–0.24	0.18–0.20
Nh/π	0.16–0.2	0.12–0.15	0.15–0.17	0.12–0.15

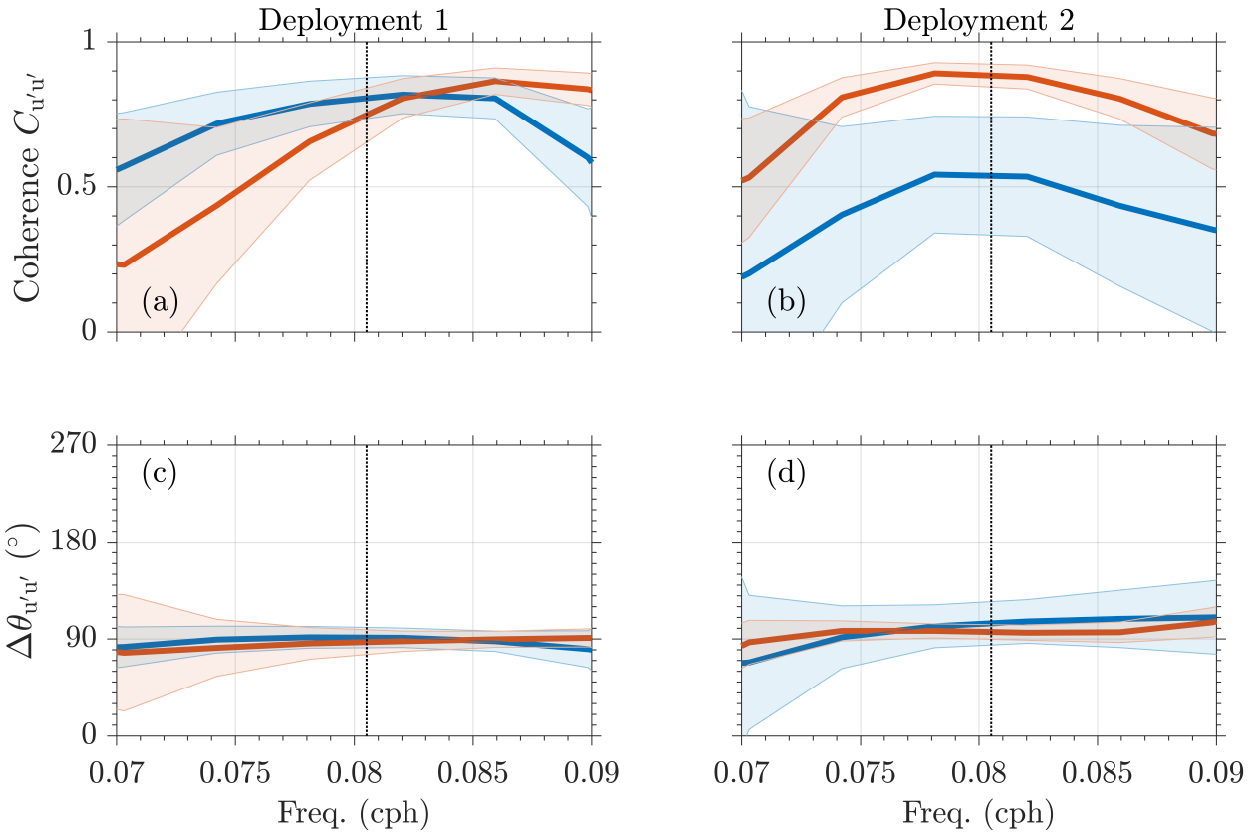

Figure 5.7: Observed (blue line) and modeled (red line) cross-shelf baroclinic velocity coherence $C_{u'u'}$ (top panels) and phase $\Delta\theta_{u'u'}$ (bottom panels) for deployment 1 (left) and deployment 2 (right) from **MS100** to **PS50**—a cross-shelf transect off Point Sal from 100m to 50m. Error bounds indicate the 95% confidence intervals. Semidiurnal frequency of ∼0.0805 cph is indicated by the black dotted line.

compared to the theoretical phase speed of a mode 1 internal wave

$$c = \frac{Nh}{\pi}$$

where N is the Brunt-Väisälä frequency and h is the water depth. Wave speeds calculated from $\Delta\theta_{u'u'}$, $\Delta\theta_{p'p'}$, and the theoretical wave speed from the cross-shelf transects of **MS100→PS50** and **PS50→PS30M** are reported in Tables 5.3 and 5.4.

From **MS100** to **PS50**, phase speeds inferred from observed $\Delta\theta_{u'u'}$ are ∼65% higher than the theoretical wave speed in deployment 1 and ∼60% higher in deployment 2 compared

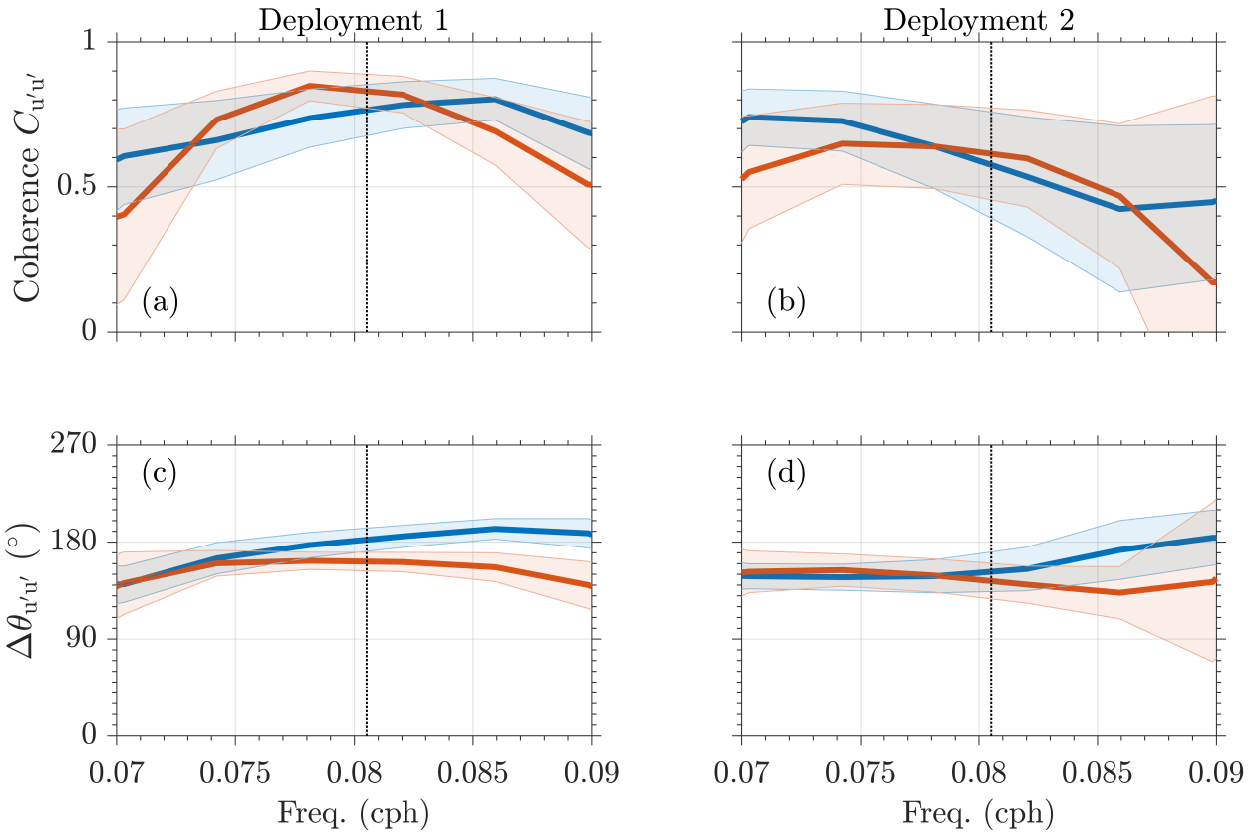

Figure 5.8: Observed (blue line) and modeled (red line) cross-shelf baroclinic velocity coherence $C_{u'u'}$ (top panels) and phase $\Delta\theta_{u'u'}$ (bottom panels) for deployment 1 (left) and deployment 2 (right) from **PS50** to **PS30M**—a cross-shelf transect off Point Sal from 50m to 30m. Error bounds indicate the 95% confidence intervals. Semidiurnal frequency of ∼0.0805 cph is indicated by the black dotted line.

to the mean. Modeled $\Delta\theta_{u'u'}$ phase speeds are ∼120% higher than the theoretical wave speed in deployment 1 and ∼100% in deployment 2. Phase speeds inferred from observed $\Delta\theta_{p'p'}$ are ∼10% higher than the theoretical wave speed in deployment 1 and ∼25% higher in deployment 2. Modeled $\Delta\theta_{u'u'}$ phase speeds are ∼80% higher than the theoretical wave speed in deployment 1 and ∼70% in deployment 2. In general in this cross-shelf transect, wave speeds calculated from $\Delta\theta_{p'p'}$ are closer to those expected from $c = \frac{Nh}{\pi}$ than for wave speeds calculated from $\Delta\theta_{u'u'}$. From **PS50** to **PS30M**, phase speeds inferred from observed $\Delta\theta_{u'u'}$

are approximately equal to the theoretical wave speed in deployment 1 and ∼15% higher in deployment 2. Modeled $\Delta\theta_{u'u'}$ phase speeds are ∼33% higher than the theoretical wave speed in deployment 1 and ∼50% in deployment 2. Phase speeds inferred from observed $\Delta\theta_{p'p'}$ are approximately equal to the theoretical wave speed in deployment 1 and ∼35% higher in deployment 2. Modeled $\Delta\theta_{u'u'}$ phase speeds are ∼33% higher than the theoretical wave speed in deployment 1 and ∼40% in deployment 2.

Wave speeds—both from $\Delta\theta$ and Nh/π—decrease from offshore to onshore as the internal tides lose energy closer to shore. In shallower waters, the modeled velocities are closer to what is observed.

5.3 Spatial Variability of the Internal Tides

The baroclinic energy fluxes feature similar spatial variability in both the cross-shelf and along shelf directions. The locations with the strongest baroclinic energy fluxes exist at 100 m offshore of the headland at Point Sal in both the observations and the model. The magnitude of the baroclinic energy fluxes decays from offshore to onshore—indicating dissipation of the internal tide—with similar e-folding scale as previous studies [*Colosi et al.*, 2018]. The cross-shore decay of internal wave energy is also seen in the propagation analysis as the internal wave speeds decrease from offshore to onshoreindicating that the internal waves slowing down upon reaching shallower waters.

Similarly, the observations and model indicate similar patterns of alongshore variability with the magnitude of baroclinic energy fluxes decaying to the north and south of the headland at Point Sal. However, the model indicates more alongshelf variability on the 50 m isobath than what is seen in the observations. This more-pronounced alongshelf variability is also seen in the model for the subtidal depth-average principal axis flow (Figure 3.1).

Chapter 6

CONCLUSIONS

An array of moored temperature and velocity measurements spanning alongshelf and cross-shelf transects in the Santa Maria Basin off the coast of Point Sal, CA is used to study temporal and spatial scales of internal tidal dynamics as part of the Office of Naval Research based innershelf DRI. The observations are complemented with a nested series of realistic, hydrostatic numerical model simulations validated against subtidal and barotropic processes to study semi-diurnal internal tidal dynamics in the mid-to-inner shelf region.

The observations indicate a cross-shelf decrease in internal tidal energy fluxes and alongshelf variation in energy decreasing in magnitude to the north and south of the rocky headland at Point Sal. Model simulations, which do not include data-assimilation or remote forcings of baroclinic information, in general are not in phase with observations and underestimate the baroclinic energy fluxes. The internal wave propagation tends to be a progressive wave in deeper waters and transitions to a partial standing wave pattern upon entering shallower waters in the inner-shelf.

BIBLIOGRAPHY

Alford, M. H., Internal swell generation: The spatial distribution of energy flux from the wind to mixed layer near-inertial motions, *Journal of Physical Oceanography*, *31*(8), 2359–2368, 2001.

Austin, J. A., and S. J. Lentz, The inner shelf response to wind-driven upwelling and downwelling, *Journal of Physical Oceanography*, *32*(7), 2171–2193, 2002.

Bendat, J. S., and A. G. Piersol, *Random data: analysis and measurement procedures*, vol. 729, John Wiley & Sons, 2011.

Boehm, A. B., B. F. Sanders, and C. D. Winant, Cross-shelf transport at huntington beach. implications for the fate of sewage discharged through an offshore ocean outfall, *Environmental science & technology*, *36*(9), 1899–1906, 2002.

Buijsman, M., Y. Uchiyama, J. McWilliams, and C. Hill-Lindsay, Modeling semidiurnal internal tide variability in the southern california bight, *Journal of Physical Oceanography*, *42*(1), 62–77, 2012.

Carter, G. S., O. B. Fringer, and E. D. Zaron, Regional models of internal tides, *Oceanography*, *25*(2), 56–65, 2012.

Chapman, D. C., Numerical treatment of cross-shelf open boundaries in a barotropic coastal ocean model, *Journal of Physical oceanography*, *15*(8), 1060–1075, 1985.

Chen, D., H. W. Ou, and C. Dong, A model study of internal tides in coastal frontal zone, *Journal of physical oceanography*, *33*(1), 170–187, 2003.

Choboter, P. F., M. Garcia, D. De Cecchis, M. Thomas, R. K. Walter, and J. E. Castillo, Nesting nonhydrostatic gccom within hydrostatic roms for multiscale coastal ocean modeling, in *OCEANS 2016 MTS/IEEE Monterey*, pp. 1–4, IEEE, 2016.

Colosi, J. A., N. Kumar, S. H. Suanda, T. M. Freismuth, and J. H. MacMahan, Statistics of internal tide bores and internal solitary waves observed on the inner continental shelf off point sal, california, *Journal of Physical Oceanography*, *48*(1), 123–143, 2018.

Cudaback, C. N., L. Washburn, and E. Dever, Subtidal inner-shelf circulation near point conception, california, *Journal of Geophysical Research: Oceans*, *110*(C10), 2005.

Dushaw, B. D., B. M. Howe, B. D. Cornuelle, P. F. Worcester, and D. S. Luther, Barotropic and baroclinic tides in the central north pacific ocean determined from long-range reciprocal acoustic transmissions, *Journal of Physical Oceanography*, *25*(4), 631–647, 1995.

Ferrari, R., and C. Wunsch, Ocean circulation kinetic energy: Reservoirs, sources, and sinks, *Annual Review of Fluid Mechanics*, *41*, 253–282, 2009.

Fewings, M., S. J. Lentz, and J. Fredericks, Observations of cross-shelf flow driven by cross-shelf winds on the inner continental shelf, *Journal of Physical Oceanography*, *38*(11), 2358–2378, 2008.

Fewings, M. R., L. Washburn, and J. C. Ohlmann, Coastal water circulation patterns around the northern channel islands and point conception, california, *Progress in Oceanography*, *138*, 283–304, 2015.

Flather, R., A tidal model of the north-west european continental shelf, *Mem. Soc. R. Sci. Liege.*, *10*, 141–164, 1976.

Frieder, C., S. Nam, T. Martz, and L. Levin, High temporal and spatial variability of dissolved oxygen and ph in a nearshore california kelp forest, *Biogeosciences*, *9*(10), 3917–3930, 2012.

Fringer, O., M. Gerritsen, and R. Street, An unstructured-grid, finite-volume, nonhydrostatic, parallel coastal ocean simulator, *Ocean Modelling*, *14*(3-4), 139–173, 2006.

Gan, J., and J. S. Allen, A modeling study of shelf circulation off northern california in the region of the coastal ocean dynamics experiment: Response to relaxation of upwelling winds, *Journal of Geophysical Research: Oceans*, *107*(C9), 6–1, 2002.

Garcia, M., P. F. Choboter, R. K. Walter, and J. E. Castillo, Validation of the nonhydrostatic general curvilinear coastal ocean model (gccom) for stratified flows, *Journal of computational science*, *30*, 143–156, 2019.

Garrett, C., and E. Kunze, Internal tide generation in the deep ocean, *Annu. Rev. Fluid Mech.*, *39*, 57–87, 2007.

Helfrich, K. R., and W. Melville, On long nonlinear internal waves over slope-shelf topography, *Journal of Fluid Mechanics*, *167*, 285–308, 1986.

Hodur, R. M., X. Hong, J. D. Doyle, J. Pullen, J. Cummings, P. Martin, and M. A. Rennick, The coupled ocean/atmosphere mesoscale prediction system (coamps), *Tech. rep.*, Naval Research Lab Monterey, CA, 2002.

Horwitz, R., and S. J. Lentz, Inner-shelf response to cross-shelf wind stress: The importance of the cross-shelf density gradient in an idealized numerical model and field observations, *Journal of Physical Oceanography*, *44*(1), 86–103, 2014.

Horwitz, R. M., and S. J. Lentz, The effect of wind direction on cross-shelf transport on an initially stratified inner shelf, *Journal of Marine Research*, *74*(4-5), 201–227, 2016.

Hüttemann, H., and K. Hutter, Baroclinic solitary water waves in a two-layer fluid system with diffusive interface, *Experiments in fluids*, *30*(3), 317–326, 2001.

Jackson, C. R., and J. Apel, An atlas of internal solitary-like waves and their properties, *Contract*, *14*(03-C), 0176, 2004.

Kerry, C. G., B. S. Powell, and G. S. Carter, Effects of remote generation sites on model estimates of m 2 internal tides in the philippine sea, *Journal of Physical Oceanography*, *43*(1), 187–204, 2013.

Kerry, C. G., B. S. Powell, and G. S. Carter, Quantifying the incoherent m2 internal tide in the philippine sea, *Journal of Physical Oceanography*, *46*(8), 2483–2491, 2016.

Kumar, N., F. Feddersen, S. Suanda, Y. Uchiyama, and J. McWilliams, Mid-to inner-shelf coupled roms–swan model–data comparison of currents and temperature: Diurnal and semidiurnal variability, *Journal of Physical Oceanography*, *46*(3), 841–862, 2016.

Kumar, N., S. S. Suanda, J. Colosi, D. Cai, K. Haas, A. Miller, C. A. Edwards, and F. Feddersen, Semidiurnal internal tide generation, propagation and transformation near pt. conception, ca: Observations and model simulations, *Journal of Geophysical Research, in review*, 2019.

Kurapov, A., J. Allen, and G. Egbert, Combined effects of wind-driven upwelling and internal tide on the continental shelf, *Journal of Physical Oceanography*, *40*(4), 737–756, 2010.

Lentz, S. J., and M. R. Fewings, The wind-and wave-driven inner-shelf circulation, *Annual review of marine science*, *4*, 317–343, 2012.

Lentz, S. J., M. Fewings, P. Howd, J. Fredericks, and K. Hathaway, Observations and a model of undertow over the inner continental shelf, *Journal of Physical Oceanography*, *38*(11), 2341–2357, 2008.

Lerczak, J. A., C. Winant, and M. Hendershott, Observations of the semidiurnal internal tide on the southern california slope and shelf, *Journal of Geophysical Research: Oceans*, *108*(C3), 2003.

Lerczak, J. A., et al., Untangling a web of interactions where surf meets coastal ocean, *Eos*, *100*, 2019.

Lucas, A. J., P. J. Franks, and C. L. Dupont, Horizontal internal-tide fluxes support elevated phytoplankton productivity over the inner continental shelf, *Limnology and Oceanography: Fluids and Environments*, *1*(1), 56–74, 2011.

MacKinnon, J. A., et al., Climate process team on internal wave–driven ocean mixing, *Bulletin of the American Meteorological Society*, *98*(11), 2429–2454, 2017.

Marchesiello, P., J. C. McWilliams, and A. Shchepetkin, Open boundary conditions for long-term integration of regional oceanic models, *Ocean modelling*, *3*(1-2), 1–20, 2001.

Martini, K. I., M. H. Alford, E. Kunze, S. M. Kelly, and J. D. Nash, Observations of internal tides on the oregon continental slope, *Journal of Physical Oceanography*, *41*(9), 1772–1794, 2011.

Mason, E., J. Molemaker, A. F. Shchepetkin, F. Colas, J. C. McWilliams, and P. Sangrà, Procedures for offline grid nesting in regional ocean models, *Ocean modelling*, *35*(1-2), 1–15, 2010.

McPhee-Shaw, E. E., D. A. Siegel, L. Washburn, M. A. Brzezinski, J. L. Jones, A. Leydecker, and J. Melack, Mechanisms for nutrient delivery to the inner shelf: Observations from the santa barbara channel, *Limnology and Oceanography*, *52*(5), 1748–1766, 2007.

Munk, W., and C. Wunsch, Abyssal recipes ii: Energetics of tidal and wind mixing, *Deep Sea Research Part I: Oceanographic Research Papers*, *45*(12), 1977–2010, 1998.

Nash, J. D., E. Kunze, J. M. Toole, and R. W. Schmitt, Internal tide reflection and turbulent mixing on the continental slope, *Journal of Physical Oceanography*, *34*(5), 1117–1134, 2004.

Nash, J. D., S. M. Kelly, E. L. Shroyer, J. N. Moum, and T. F. Duda, The unpredictable nature of internal tides on continental shelves, *Journal of Physical Oceanography*, *42*(11), 1981–2000, 2012a.

Nash, J. D., E. L. Shroyer, S. M. Kelly, M. E. Inall, T. F. Duda, M. D. Levine, N. L. Jones, and R. C. Musgrave, Are any coastal internal tides predictable?, *Oceanography*, *25*(2), 80–95, 2012b.

Omand, M. M., J. J. Leichter, P. J. Franks, R. Guza, A. J. Lucas, and F. Feddersen, Physical and biological processes underlying the sudden surface appearance of a red tide in the nearshore, *Limnology and Oceanography*, *56*(3), 787–801, 2011.

Osborne, A., T. Burch, R. Scarlet, et al., The influence of internal waves on deep-water drilling, *Journal of Petroleum Technology*, *30*(10), 1–497, 1978.

Pawlowicz, R., B. Beardsley, and S. Lentz, Classical tidal harmonic analysis including error estimates in matlab using t_tide, *Computers & Geosciences*, *28*(8), 929–937, 2002.

Pickering, A., M. Alford, J. Nash, L. Rainville, M. Buijsman, D. S. Ko, and B. Lim, Structure and variability of internal tides in luzon strait, *Journal of Physical Oceanography*, *45*(6), 1574–1594, 2015.

Pineda, J., Predictable upwelling and the shoreward transport of planktonic larvae by internal tidal bores, *Science*, *253*(5019), 548–549, 1991.

Ramp, S. R., T. Y. Tang, T. F. Duda, J. F. Lynch, A. K. Liu, C.-S. Chiu, F. L. Bahr, H.-R. Kim, and Y.-J. Yang, Internal solitons in the northeastern south china sea. part i: Sources and deep water propagation, *IEEE Journal of Oceanic Engineering*, *29*(4), 1157–1181, 2004.

Rayson, M. D., G. N. Ivey, N. L. Jones, M. J. Meuleners, and G. W. Wake, Internal tide dynamics in a topographically complex region: Browse basin, australian north west shelf, *Journal of Geophysical Research: Oceans*, *116*(C1), 2011.

Roder, C., L. Fillinger, C. Jantzen, G. M. Schmidt, S. Khokiattiwong, and C. Richter, Trophic response of corals to large amplitude internal waves, *Marine Ecology Progress Series*, *412*, 113–128, 2010.

Savidge, D. K., C. R. Edwards, and M. Santana, Baroclinic effects and tides on the cape hatteras continental shelf, *Journal of Geophysical Research: Oceans*, *112*(C9), 2007.

Shchepetkin, A. F., and J. C. McWilliams, The regional oceanic modeling system (roms): a split-explicit, free-surface, topography-following-coordinate oceanic model, *Ocean modelling*, *9*(4), 347–404, 2005.

Shchepetkin, A. F., and J. C. McWilliams, Correction and commentary for ocean forecasting in terrain-following coordinates: Formulation and skill assessment of the regional ocean modeling system by haidvogel et al., j. comp. phys. 227, pp. 3595–3624, *Journal of Computational Physics*, *228*(24), 8985–9000, 2009.

Sherwin, T., Analysis of an internal tide observed on the malin shelf, north of ireland, *Journal of Physical Oceanography*, *18*(7), 1035–1050, 1988.

Shroyer, E. L., J. N. Moum, and J. D. Nash, Mode 2 waves on the continental shelf: Ephemeral components of the nonlinear internal wavefield, *Journal of Geophysical Research: Oceans*, *115*(C7), 2010.

Simmons, H. L., R. W. Hallberg, and B. K. Arbic, Internal wave generation in a global baroclinic tide model, *Deep Sea Research Part II: Topical Studies in Oceanography*, *51*(25-26), 3043–3068, 2004.

Sinnett, G., F. Feddersen, A. J. Lucas, G. Pawlak, and E. Terrill, Observations of nonlinear internal wave run-up to the surfzone, *Journal of Physical Oceanography*, *48*(3), 531–554, 2018.

Suanda, S., J. Barth, and C. Woodson, Diurnal heat balance for the northern monterey bay inner shelf, *Journal of Geophysical Research: Oceans*, *116*(C9), 2011.

Suanda, S. H., and J. A. Barth, Semidiurnal baroclinic tides on the central oregon inner shelf, *Journal of Physical Oceanography*, *45*(10), 2640–2659, 2015.

Suanda, S. H., F. Feddersen, and N. Kumar, The effect of barotropic and baroclinic tides on coastal stratification and mixing, *Journal of Geophysical Research: Oceans*, *122*(12), 10,156–10,173, 2017.

Suanda, S. H., et al., Wind relaxation and a coastal buoyant plume north of pt. conception, ca: Observations, simulations, and scalings, *Journal of Geophysical Research: Oceans*, *121*(10), 7455–7475, 2016.

Thyng, K. M., C. A. Greene, R. D. Hetland, H. M. Zimmerle, and S. F. DiMarco, True colors of oceanography: Guidelines for effective and accurate colormap selection, *Oceanography*, *29*(3), 9–13, 2016.

Vitousek, S., and O. B. Fringer, Physical vs. numerical dispersion in nonhydrostatic ocean modeling, *Ocean Modelling*, *40*(1), 72–86, 2011.

Vlasenko, V., and K. Hutter, Generation of second mode solitary waves by the interaction of a first mode soliton with a sill, *Nonlinear Processes in Geophysics*, *8*(4/5), 223–239, 2001.

Walter, R. K., C. B. Woodson, P. R. Leary, and S. G. Monismith, Connecting wind-driven upwelling and offshore stratification to nearshore internal bores and oxygen variability, *Journal of Geophysical Research: Oceans*, *119*(6), 3517–3534, 2014.

Washburn, L., M. R. Fewings, C. Melton, and C. Gotschalk, The propagating response of coastal circulation due to wind relaxations along the central california coast, *Journal of Geophysical Research: Oceans*, *116*(C12), 2011.

Waterhouse, A. F., J. A. Mackinnon, R. C. Musgrave, S. M. Kelly, A. Pickering, and J. Nash, Internal tide convergence and mixing in a submarine canyon, *Journal of Physical Oceanography*, *47*(2), 303–322, 2017.

Waterhouse, A. F., et al., Global patterns of diapycnal mixing from measurements of the turbulent dissipation rate, *Journal of Physical Oceanography*, *44*(7), 1854–1872, 2014.

Waterhouse, A. F., et al., Observations of the tasman sea internal tide beam, *Journal of Physical Oceanography*, *48*(6), 1283–1297, 2018.

Whalen, C., J. MacKinnon, and L. Talley, Large-scale impacts of the mesoscale environment on mixing from wind-driven internal waves, *Nature Geoscience*, *11*(11), 842, 2018.

Winters, K. B., P. N. Lombard, J. J. Riley, and E. A. D'Asaro, Available potential energy and mixing in density-stratified fluids, *Journal of Fluid Mechanics*, *289*, 115–128, 1995.

Woodson, C., The fate and impact of internal waves in nearshore ecosystems, *Annual review of marine science*, *10*, 421–441, 2018.

Wunsch, C., and R. Ferrari, Vertical mixing, energy, and the general circulation of the oceans, *Annu. Rev. Fluid Mech.*, *36*, 281–314, 2004.

Zhao, Z., M. H. Alford, J. A. MacKinnon, and R. Pinkel, Long-range propagation of the semidiurnal internal tide from the hawaiian ridge, *Journal of Physical Oceanography*, *40*(4), 713–736, 2010.